9-9-2007

Cramer-Rao bound analysis of multi-frame blind deconvolution

Alim Haji

Alim Haji
Candidate

Optical Science and Engineering
Department

This thesis is approved, and it is acceptable in quality and form for publication on microfilm:

Approved by the Thesis Committee:

, Chairperson

Accepted:

Dean, Graduate School

Date

CRAMER-RAO BOUND ANALYSIS OF MULTI-FRAME BLIND DECONVOLUTION

BY

ALIM HAJI

B.S. Computer Engineering, University of New Mexico, 2004

THESIS

Submitted in Partial Fulfillment of the
Requirements for the Degree of

Master of Science
Optical Science and Engineering

The University of New Mexico
Albuquerque, New Mexico

May, 2007

Dedication

This thesis is dedicated to my parents, Shiraz and Yasmin Haji. Their unwavering effort and determination to provide me with the opportunity to pursue my education has made this possible.

Acknowledgments

I would like to express sincere appreciation to my advisor, Dr. Charles Matson. First and foremost, the work and completion of this thesis would not have been possible without his decision to accept me as a student intern into his group. Also, he constantly supported, motivated and challenged me throughout the course of the research and writing of this thesis.

I would like to acknowledge the U.S. Air Force Research Laboratory for providing me with the opportunity to perform my research in a top-notch facility.

I would also like to thank Mr. Charles Beckner. The time and knowledge he gave was invaluable. His continuous advice, guidance and encouragement facilitated my entire experience at the U.S. Air Force Research Laboratory.

Last but not least, I would like to offer my gratitude to Dr. Marek Osinski of the Optical Science and Engineering program at the University of New Mexico for considering and recommending me for the internship opportunity.

CRAMER-RAO BOUND ANALYSIS OF MULTI-FRAME BLIND DECONVOLUTION

BY

ALIM HAJI

ABSTRACT OF THESIS

Submitted in Partial Fulfillment of the
Requirements for the Degree of

Master of Science
Optical Science and Engineering

The University of New Mexico
Albuquerque, New Mexico

May, 2007

CRAMER-RAO BOUND ANALYSIS OF
MULTI-FRAME BLIND DECONVOLUTION

BY

ALIM HAJI

B.S., Computer Engineering, University of New Mexico, 2004
M.S., Optical Science and Engineering, University of New Mexico, 2007

ABSTRACT

This thesis explores how support constraints and multiple frames affect multi-frame blind deconvolution. Previous research in non-blind deconvolution, which seeks to estimate an object from a blurred and noisy image, characterized how the use of support constraints exploited spatial noise correlations to reduce noise in the estimate of the object. In multi-frame blind deconvolution, the blurring function is unknown and must be estimated along with the object. Applying a support constraint to both the object and the blurring functions, when using blind deconvolution, is one way to ensure a unique solution. The effects on the estimate of the object as a function of the size of the supports are analyzed. Also, the benefit in noise reduction in the estimate of the object from including multiple blurred and noisy images is considered. Cramer-Rao Bound theory is employed to provide an algorithm-independent metric to analyze the effects from these parameters. The Cramer-Rao bound is a lower limit to the variance of any estimate of an unknown parameter. In this research, the unknown parameters are the intensities of the object which is estimated.

Table of Contents

List of Figures

List of Tables

1. INTRODUCTION

The aim of reconstruction in image processing is to restore an object from blurred and noisy data. This reconstruction process is useful for many fields such as astronomical imaging [1], medical imaging [2,3], remote sensing [4], etc. The classical image restoration problem is one of deconvolving a known blurring function with the blurred data. In some situations, the blurring function is either known *a priori* or can be estimated accurately from additional measurements.

In many practical imaging situations, however, it is impossible to know or estimate the blurring function separately from the object restoration process [5]. At best, information about the blurring, such as the support [6], may be available. Thus, a need to estimate the object without explicit knowledge of the blurring function is present. Multi-frame blind deconvolution (MFBD) algorithms exist to solve this problem. The term multi-frame refers to the use of multiple blurred and noisy measurements in the reconstruction process. The term blind denotes that the blurring function is unknown, as opposed to the classical non-blind case in which the blurring function is known. Thus, multi-frame blind deconvolution algorithms reconstruct an object by estimating the true

intensity from many blurred and noisy measurement frames. Applying a prior knowledge constraint, such as a support constraint, is one way for the algorithm to achieve a unique solution. Also, a reasonable model for the noise characteristics is required. Below is a block representation of the MFBD process.

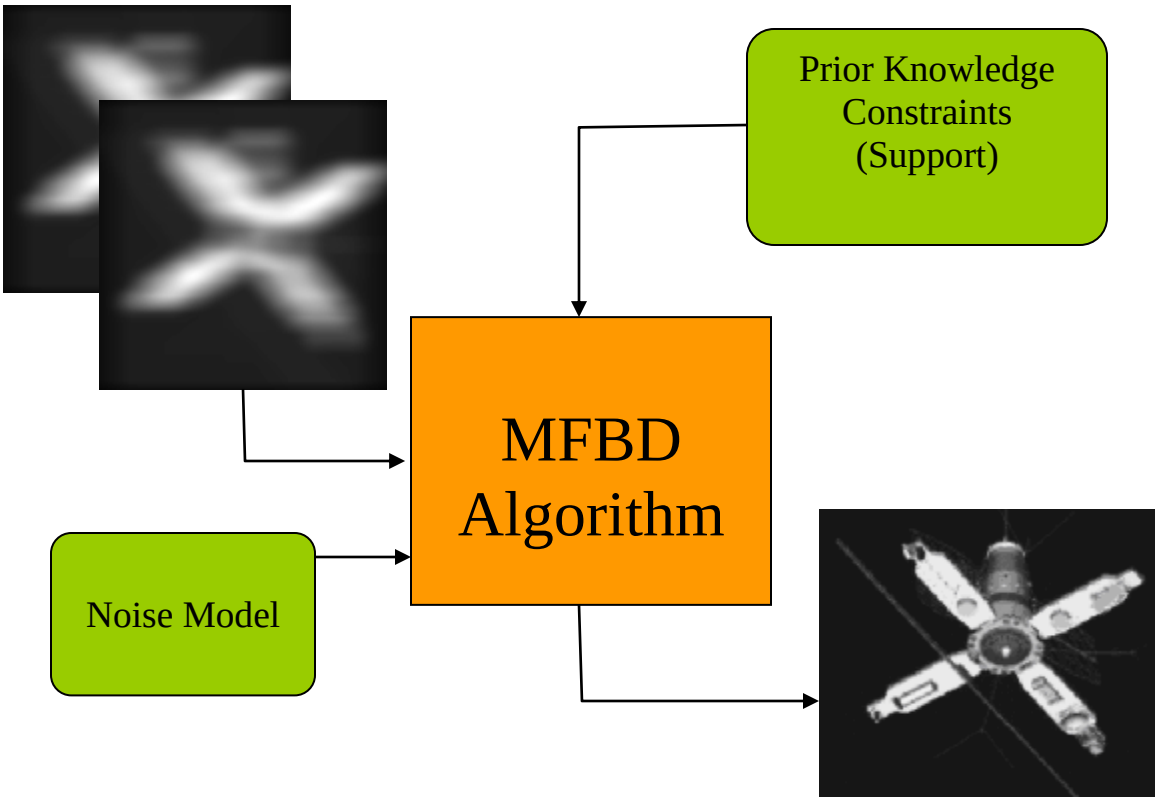

Figure 1. Block diagram of the multi-frame blind deconvolution process

Previous work in non-blind deconvolution presented in [7] explored the benefits of applying a support constraint. It was shown that using the tightest support produced the best results. Furthermore, the largest noise reduction was always possible at the edges of the support.

The research for this thesis is an extension to MFBD of the work in non-blind deconvolution. The purpose is to understand MFBD as a function of its input parameters. In this thesis, the effects on the quality of the reconstruction of an object as a function of two parameters are presented. These parameters are the support constraint, for both the object and blurring functions, and the use of multiple measurement frames in the reconstruction process. The reconstruction quality is measured in terms of the variance of the intensities of the restored object. Using variance may seem problematic because reconstructions from any two MFBD algorithms may produce different variances for the same set of parameters. Therefore, in order to analyze the effects from the parameters themselves, and not the effects of specific algorithms, an algorithm-independent metric is necessary. The Cramer-Rao inequality has been chosen to provide this algorithm-independent metric [8]. This inequality expresses the lower limit to the variance of the estimate of an unknown parameter as a function of a given set of constraints [9]. In the case of this research, the unknown parameters are the object intensity values that are to be estimated. Although the Cramer-Rao inequality does not specify the algorithm that achieves this lower limit, or does not even specify if the lower limit is achievable, it provides a lower bound that can be used for comparisons. In the research for this thesis, the Cramer-Rao Bound (CRB) is the metric used to compare the effects from different MFBD parameters.

The thesis is divided among the following five chapters. First, a background chapter that describes the theory behind the research is presented. Next, a description of all the reconstruction parameters common to the results in the research is given. Finally,

the results are presented in two chapters, followed by a summary and discussion of the conclusions in the last chapter.

The first results chapter is the extension of the work presented in [7] to blind deconvolution. Blind deconvolution CRBs as a function of the size of the object support constraints are compared to non-blind CRBs using the same constraints. It is shown that the blind deconvolution CRBs for the given support are always greater than the non-blind CRBs. In addition, the morphologies of blind deconvolution CRBs differ from the morphologies of non-blind CRBs.

The second results chapter focuses on the MFBD CRBs from variations of two parameters that were not explored in [7]. These parameters are the blurring function support constraint and the inclusion of multiple measurement frames. First, the role that the size of the blurring function support constraint plays on the blind deconvolution CRBs is explored. It is shown that the impact on the CRBs is not as significant as the impact from the size of the object support. Second, the decrease in CRBs as a function of the number of measurement frames is analyzed. It is shown that as more frames are included, the CRBs of the object decrease. Furthermore, the most decrease is seen with the inclusion of the first few frames. The magnitude of this decrease is heavily dominated by properties of the actual blurring function. As more frames are included, the decrease in CRBs conforms to a simple mathematical model.

Parts of the results presented in this thesis were published in [10].

2. BACKGROUND

This chapter seeks to introduce the theory behind the two fundamental concepts employed in the research: the imaging model and Cramer-Rao Bound theory. First, the imaging model will be explained along with the concepts behind image reconstruction. The reconstruction model consists of three components: the point spread function, a noise model, and a prior knowledge constraint. These ideas are all explained in further detail. Second, the theory of Cramer-Rao Bounds is presented. These bounds provide an algorithm-independent lower-limit on the variance of an estimator. The results presented in the thesis are based on the CRB calculations for various imaging scenarios.

2.1. Imaging Model

The imaging model used in the rest of the thesis consists of three components and is given by the equation,

$$i(\mathbf{x}) = o(\mathbf{x}) * h(\mathbf{x}) + n(\mathbf{x}), \qquad (1)$$

where $i(\mathbf{x})$ is a blurred and noisy image, $\mathbf{x}$ is a two-dimensional vector representing the position in image space, $o(\mathbf{x})$ is the true object that is being imaged, and $h(\mathbf{x})$ is the point-spread function (PSF) that blurs each point in the object. The convolution operator that

blurs the PSF with the object is represented by an asterisk. There is also an additive noise term included in the imaging model. This noise term is represented by $n(\mathbf{x})$. Further details on these components are given below.

2.1.1. Point Spread Function

The point-spread function represents how an object is blurred when being imaged. This blurring can be caused by several factors. In this thesis the effects of the atmosphere will be modeled in the PSF. The PSF does not simply multiply with the object, but rather each point in the object is blurred the same. This is embodied in the equation:

, (2)

where x_1 and x_2 are the components of the vector $\mathbf{x}$ from Eq. (1). For convenience the above convolution operation will be denoted by an asterisk. The convolution model is incomplete as it does not include a noise term.

The PSF is represented by simply dividing up the intensities of the PSF over a square grid. Each square is known as a pixel and stores the intensity integrated over the area of that pixel. This model is typical of how a CCD camera captures an image or how a digital image is stored on a computer [11]. This representation is intuitive and allows the results to easily be displayed.

2.1.2. Noise Model

The imaging model in Eq. (1) includes an additive noise term that represents the effects of various types of noise introduced when capturing the image. This additive term sufficiently models the noise in CCD cameras. A model for the noise present in CCD cameras will be discussed here. It is assumed that the noise is zero-mean and statistically independent from pixel to pixel [12].

A CCD photo-detector is a 2-dimensional array of pixels in which a charge accumulates during the exposure interval. The charge value is read out of each pixel from a serial register, row by row, until all the pixels are read. CCD cameras exhibit noise and further distort the blurred image [13].

There are several sources of noise inherent when using CCD cameras. However, only one of these noise sources is modeled for the research in this thesis. The model is known as read noise and is based on the noise that is present when amplifying the output of the CCD array before the analog-to-digital conversion. Thus, the characteristics of the noise model are independent of the signal at each pixel.

When the information in each capacitor is read, the analog value is converted into a digital value. This process inherently introduces noise. Since every pixel in the CCD array is transferred, the noise is present at every pixel. The noise does not depend on the signal at that pixel. This noise is modeled well with the Gaussian distribution which is given by

$$P(n) = \frac{1}{\sqrt{2\pi\sigma}} \exp\left[-\frac{(n-a)^2}{2\sigma}\right], \qquad (3)$$

where a is the mean and σ is the variance of the Gaussian distribution. Thus, the function P gives the probability density function of the read noise. In order to be able to simply add the noise term to the imaging model, the mean, a, is set to zero.

2.2. Reconstruction

The forward imaging model presented in Eq. (1) can be inverted to obtain the object from the image. This is the basis of image reconstruction. This section will introduce the concepts of reconstruction used in the rest of the thesis. First, the Fourier representation of the imaging model is described. Next, the simplest method of deconvolution without noise is presented. Finally, noise correlations along with various prior knowledge constraints are explained.

2.2.1. Fourier Representation

The forward imaging model is represented in the frequency domain by the equation:

$$I(\mathbf{f}) = H(\mathbf{f})\,O(\mathbf{f}) + N(\mathbf{f}) \quad , \qquad (4)$$

where $\mathbf{f}$ is a two-dimensional vector that represents the spatial frequencies, and the upper-case letters represent the Fourier transforms of the their respective lower-case counterparts in Eq. (1). The Fourier transform of the PSF is also known as the optical transfer function (OTF) [14]. Note that in the Fourier domain the convolution is

substituted by a multiplication operation [15]. This substitution allows us to complete a simple reconstruction which is described in the next section.

2.2.2. Deconvolution

Deconvolution is the act of separating the point spread function from the true object. This is used to obtain the object estimate. First, deconvolution in the non-blind case is considered. Non-blind deconvolution assumes that the PSF of the system is known. In the absence of noise, deconvolution can be achieved by simply dividing the Fourier transform of the image by the Fourier transform of the known PSF. This is shown in by

$$\hat{O}(\mathbf{f}) = \frac{I(\mathbf{f})}{H(\mathbf{f})} = \frac{O(\mathbf{f})\,H(\mathbf{f})}{H(\mathbf{f})} = O(\mathbf{f}) \ , \tag{5}$$

where $\hat{O}(\mathbf{f})$ represents the Fourier transform of the object estimate. The underlying assumption here is that the Fourier transform of the PSF is invertible. Thus, the original object is fully reclaimed if the above assumption is made. To make the problem more realistic, the noise term is included. This results in the following equations:

$$I(\mathbf{f}) = O(\mathbf{f})\,H(\mathbf{f}) + N(\mathbf{f}) \ ,$$

$$\hat{O}(\mathbf{f}) = \frac{I(\mathbf{f})}{H(\mathbf{f})} = \frac{O(\mathbf{f})\,H(\mathbf{f})}{H(\mathbf{f})} + \frac{N(\mathbf{f})}{H(\mathbf{f})} = O(\mathbf{f}) + \frac{N(\mathbf{f})}{H(\mathbf{f})} \ . \tag{6}$$

The inverse Fourier transform of Eq. (6) yields the equation,

$$\hat{o}(\mathbf{x}) = o(\mathbf{x}) + h_{inv}(\mathbf{x}) * n(\mathbf{x}) \tag{7}$$

which shows that the original noise term is now convolved with the function, h_{inv}, that corresponds to the inverse Fourier transform of the inverse OTF. It was shown in Section 2.1.2 that the original noise term is spatially-uncorrelated. However, the convolution of h_{inv} with the original noise term creates spatial correlations in the noise. It was shown in [6] that these correlations are necessary for the reduction of noise in the object estimate.

In the case of blind deconvolution, the PSF is not known. As a result, the deconvolution cannot be carried out explicitly since no closed-form solution exists as in the non-blind case. However, deconvolution can be achieved through iterative methods [16].

2.2.3. Prior Knowledge

The final component of the MFBD process is a prior knowledge constraint. Prior knowledge constraints have been shown to be effective in deconvolution [6,7]. In the research, only the support constraint is considered.

A support constraint is utilized by defining an area around the blurred object where it is certain that there is no signal outside the region. Thus, any artifacts outside the support region must be noise. Since convolving the additive noise term by the inverse of the OTF correlates the pixels in the object, knowledge that the signal is zero outside the support can be used to remove noise from inside the support. An example is presented in Section 2.3.3.

2.3. Cramer-Rao Bound

The Cramer-Rao Bound (CRB) expresses a lower limit to the variance of any unbiased estimator [18]. An estimator is a mathematical function that seeks to estimate an unknown parameter from a set of noisy data. Since the estimator is based on the data which is random in nature, the estimator itself is a random variable. Therefore, in order to judge the quality of an estimator, the variance of the estimates is calculated. Thus, an estimator of a parameter that produces estimates that have lower variance than another estimator is said to be better. Again, the CRB computes the lower bound to the variance of any estimator. It is important to note that this variance may not necessarily be an achievable quantity. Even so, the CRB provides a benchmark to which an actual estimator can be compared.

In the case of the imaging problem for the research, the unknown parameters are the true object intensities being estimated from the blurred and noisy measurements. The results in the thesis are based on the comparison of CRBs for different reconstruction parameters, such as the size of the support constraint, and the inclusion of multiple measurement frames. Comparing the CRBs allows for comparison of the effects of these parameters on the image reconstruction regardless of how a specific estimator algorithm implements the reconstruction.

2.3.1. Formulation

Since many intensities of the object are estimated, the CRB is calculated for a vector of parameters. First, the original imaging equation must be transformed from continuous to discrete form. This is presented in the equation:

(8)

where α is a two-dimensional array that has replaced the continuous variable **x** from Eq. (1). Also, the convolution integral in Eq. (2) is transformed into a convolution summation given by the equation,

$$i(\alpha) = \sum_{t} h(\alpha - t)\, o(t) \ , \tag{9}$$

where *h* is the PSF and *o* is the object. The summation is performed over all the elements in α.

Additionally, Eq. (8) needs to be further modified to vector form. This is accomplished by stacking the columns of *o(α)* and *n(α)*. *h(α)* and the convolution operation also need to be transformed into vector form. Simply stacking the columns of *h(α)* and multiplying by *o(α)* does not correctly compute the convolution operation. Instead, *h(α)* needs to be transformed into a block circulant matrix. This matrix, when multiplied with the stacked columns of *o(α)* will produce a stacked-column vector equivalent to the stacked-column vector of *h(α)* convolved with *o(α)*. Eq. (8) replaced by its vector counterparts is shown below:

$$\mathbf{y} = \mathbf{H}\boldsymbol{\theta} + \boldsymbol{\eta} \ , \tag{10}$$

where **y**, **θ** and **η** are formed by stacking the columns of *i(α) o(α)* and *n(α)*, respectively. The matrix **H** is a square matrix with elements given by the elements of the convolution operation [17].

2.3.2. Cramer-Rao Inequality

The CRB for a scalar parameter, θ, is given by the following inequality:

$$Var(\theta) \geq \frac{1}{-E\left[\frac{\partial^2 \ln\ p(n;\theta)}{\partial \theta^2}\right]}, \tag{11}$$

where $p(n;\theta)$ is a probability density function (PDF) parameterized on the unknown variable θ. The operator, E, represents the expected value. According to the above equation the variance of the estimate will always be greater than or equal to the inverse of the average curvature of the log-likelihood function. Note that the PDF must be known to find the CRB of the estimate. All the information is contained in the observed data and the PDF for those data [18].

The CRB inequality can be extended to vector form. Assume the parameters $\boldsymbol{\theta} = [\theta_1\ \theta_2\ \ldots\ \theta_n]$ are to be jointly estimated. If the joint PDF is known, then the CRBs for each of the unknown parameters are given by the equation

$$\mathbf{V}(\boldsymbol{\theta}) \geq [\mathbf{F}(\boldsymbol{\theta})]^{-1}, \tag{12}$$

where F is the Fisher Information Matrix (FIM) given by

$$[F(\theta)]_{ij} = -E\left[\frac{\partial^2 \ln\ p(n;\theta)}{\partial \theta_i\ \partial \theta_j}\right]. \tag{13}$$

Thus, the CRBs are located on the diagonals of the inverse of the FIM.

As in the scalar case, the joint PDF must be known. For the imaging model given in Eq. (1), we see that the PDF depends only on the additive noise model. Therefore, the probability density function is given by

$$p(n;\theta) = \tilde{p}(\boldsymbol{\eta}) = \tilde{p}(\mathbf{y} - \mathbf{H}\boldsymbol{\theta}) \ , \tag{14}$$

where $\tilde{p}$ is the PDF of the read noise term given in Eq. (3). The PDF of the measurement is equal to the PDF of the noise with a non-zero mean equal to the intensity of the blurred object.

There exist problems of uniqueness in blind deconvolution when calculated the CRBs. One problem is that if the object estimate is multiplied by a constant factor and the PSF estimate is multiplied by the inverse of that factor, then the solution without the factors is still given. Furthermore, an infinite number of factors exist and therefore, an infinite number of solutions exist. This is described in the equation below.

$$\begin{aligned} i(\mathbf{x}) &= o(\mathbf{x}) * h(\mathbf{x}) = \left[\frac{1}{K} o(\mathbf{x})\right] * \left[K\, h(\mathbf{x})\right] \ , \\ I(\mathbf{f}) &= \left(\frac{1}{K} O(\mathbf{f})\right)\left(K\ H(\mathbf{f})\right) = O(\mathbf{f})\, H(\mathbf{f}) \ . \end{aligned} \tag{15}$$

where K is a multiplicative factor and the uppercase letters represent the Fourier transform of their respective lowercase counterparts. To avoid this degeneracy, instead of calculating the CRBs for each element in the object and PSF, one less element in each can be calculated. The element not estimated is then given by

, (16)

where $\mathbf{x}_N$ is the uncalculated element and dc_{obj} is the total intensity of the image.

The other uniqueness problem stems from the fact that multiple solutions exist by shifting the object estimate within the support in one direction and equally shifting the PSF in the opposite direction. This is described in the following equations:

$$\begin{aligned} i(\mathbf{x}) &= o(\mathbf{x}) * h(\mathbf{x}) = o(\mathbf{x}-\mathbf{a})\, h(\mathbf{x}+\mathbf{a}) \quad , \\ I(\mathbf{f}) &= \left(O(\mathbf{f})\, e^{-j2\pi \mathbf{f}\,\mathbf{a}}\right)\left(H(\mathbf{f})\, e^{j2\pi \mathbf{f}\,\mathbf{a}}\right) = O(\mathbf{f})\, H(\mathbf{f}) \quad . \end{aligned} \tag{17}$$

where **a** is a two-dimensional shift vector. If the object and PSF are shifted the same distance in opposite directions, the two exponential terms in the Fourier domain equation multiply to 1. To avoid this degeneracy, the CRBs were calculated by enforcing perfect support on either the object or PSF in all calculations. Since the estimates of the object and PSF exist only in the support region, enforcing perfect support on either the object or PSF ensures that the estimate cannot be shifted.

2.3.3. Fisher Information Matrix

The Fisher Information Matrix (FIM) is a measure of the information that an observable random variable carries about an unobservable parameter [9]. In the case of blind-deconvolution CRBs, we are interested in the estimates of the object and PSF from multiple measurement frames. The content of the FIM is based on measurement frame data and the applied support.

The purpose of this section is to give the reader necessary detail on how to construct the FIM for our problem of interest. This is important in order to understand how the parameters, such as support, are implemented in the CRB calculations. A basic

example of how the noise correlations are exploited by applying a support constraint is presented. Also, the size of the FIM for the blind deconvolution case poses a computational problem. The problem is explored in detail in this section.

a. Structure

As shown in the previous section, the elements of the FIM are given by the following equation:

$$\left[F(\boldsymbol{\theta})\right]_{ij} = -E\left[\frac{\partial^2 \ln\ p(n;\boldsymbol{\theta})}{\partial\theta_i\ \partial\theta_j}\right] . \tag{18}$$

For simplicity, the FIM structure is given first for the non-blind case, where only the object intensities are estimated. The FIM is given by

$$\mathbf{F_{obj}} = \begin{bmatrix} f_{11} & f_{12} & . & . & f_{1N} \\ f_{21} & f_{22} & & & \\ . & & . & & \\ . & & & . & \\ f_{N1} & & & & f_{NN} \end{bmatrix} , \tag{19}$$

where N is the number of pixels in the object support. The elements are given by Eq. (18). The diagonal elements represent the sensitivity of a parameter to a change in itself, while the off-diagonal elements, f_{ij}, represent the sensitivity of one parameter, θ_i, to a change in another parameter, θ_j.

The structure of the FIM is now posed to include **M** measurement frames.

$$\mathbf{F} = \begin{bmatrix} \mathbf{F_{11}} & \mathbf{F_{12}} & \cdot & \cdot & \cdot & \mathbf{F_{1M}} \\ \mathbf{F_{21}} & \mathbf{F_{22}} & & & & \\ \cdot & & \cdot & & & \\ \cdot & & & \cdot & & \\ \cdot & & & & \cdot & \\ \mathbf{F_{M1}} & & & & & \mathbf{F_{MM}} \end{bmatrix}, \qquad (20)$$

where each $\mathbf{F_{ij}}$ represents a block matrix. Specifically, $\mathbf{F_{11}}$ is the block given by $\mathbf{F_{obj}}$ in Eq. (19). For each PSF frame, **m**, included in the reconstruction, three additional blocks is added to **F**. $\mathbf{F_{mm}}$ is added to the diagonal, while $\mathbf{F_{1m}}$ and $\mathbf{F_{m1}}$ are added to the first row and first column, respectively. Besides the elements in the first row, first column and the diagonal, the other elements of **F** are zero. The elements in the non-zero blocks, $\mathbf{F_{i1}}$, $\mathbf{F_{1i}}$, and, $\mathbf{F_{ii}}$, are given by the following equations:

$$[\mathbf{F}_{11}]_{kj} = \sum_{m=1}^{M} \sum_{\mathbf{x}} \frac{\left[h_m(\mathbf{x}-\mathbf{x}_k) - h_m(\mathbf{x}-\mathbf{x}_N)\right]\left[h_m(\mathbf{x}-\mathbf{x}_j) - h_m(\mathbf{x}-\mathbf{x}_N)\right]}{\sigma^2(\mathbf{x})}, \qquad (21)$$

$$[\mathbf{F}_{i1}]_{kj} = [\mathbf{F}_{1i}]_{kj} = \sum_{\mathbf{x}} \frac{\left[h_i(\mathbf{x}-\mathbf{x}_k) - h_i(\mathbf{x}-\mathbf{x}_N)\right]\left[o(\mathbf{x}-\mathbf{x}_j) - o(\mathbf{x}-\mathbf{x}_N)\right]}{\sigma^2(\mathbf{x})}, \qquad (22)$$

$$[\mathbf{F}_{ii}]_{kj} = \sum_{\mathbf{x}} \frac{\left[o(\mathbf{x}-\mathbf{x}_k) - o(\mathbf{x}-\mathbf{x}_N)\right]\left[o(\mathbf{x}-\mathbf{x}_j) - o(\mathbf{x}-\mathbf{x}_N)\right]}{\sigma^2(\mathbf{x})}, \qquad (23)$$

where $o(\mathbf{x})$ represents the object elements, $h_m(\mathbf{x})$ each PSF frame, and σ^2 the read noise variance. The subscripts, *1i*, *i1* and, *ii*, represent blocks of the FIM, and the subscripts, *k* and *j*, represent elements of that block. Recall from Section 2.3.2 that in order to avoid the scaling degeneracy, one intensity location from the object and each PSF frame is not calculated. This intensity location is represented by $\mathbf{x}_N$ in the equations above.

Even for the non-blind case shown in Eq. (19) the FIM can become large. For example, an object with (n x n) pixels will result in a stacked vector of n^2 elements. The FIM will consist of n^2 elements on the diagonal, which translates to a FIM of size (n^2 x n^2). This results in a total of n^4 elements in the FIM.

Additionally, when estimating the PSFs along with the object, the total number of diagonal elements is given by

$$S = (\mathbf{M} + 1) \cdot n^2 \quad , \tag{24}$$

where S is the number of diagonal elements, n^2 is the number of intensity values in each measurement frame and $\mathbf{M}$ is the number of frames included.

With typical values for m and n, the size of the FIM is given by the equations:

$$\begin{aligned} &\mathbf{M} = 10; n = 64 \quad , \\ &S = (10 + 1) \cdot 64^2 = 45056 \quad , \\ &S^2 = 2,030,043,136 \quad , \end{aligned} \tag{25}$$

which results in 45056 elements in the diagonal for a total of 2030043136 elements in the FIM! Since the matrix must be inverted to obtain the CRBs there is clear motivation to reduce the size of the FIM.

b. FIM with Support

One way to reduce the number of elements in the FIM is to apply a support constraint to the object and PSF frames. For elements outside the support region, the corresponding rows and columns can be set to zero. However, with zero-elements on the

diagonal, a pseudo-inverse of the FIM must be applied. This can be accomplished by inverting the non-zero sub-matrix and reinserting into the FIM.

For example, consider a two-pixel object, $\boldsymbol{\theta} = [\theta_1, \theta_2]$, that is to be estimated. Assume that only read noise is present. The noise has a uniform variance of σ^2 for both pixels. The FIM can be calculated using Eq. (18) and the jointly-normal PDF given by

$$p(n;\boldsymbol{\theta}) = \frac{1}{2\pi\sigma^2\sqrt{1-\rho^2}} \cdot \exp\left[-\frac{1}{2}(n-\boldsymbol{\theta})^T C^{-1}(n-\boldsymbol{\theta})\right], \tag{26}$$

where ρ is the correlation coefficient between the two pixels and $\mathbf{C}$ is the covariance matrix between the two pixels. The covariance matrix is given by

$$\mathbf{C} = \begin{bmatrix} \sigma^2 & \rho\sigma^2 \\ \rho\sigma^2 & \sigma^2 \end{bmatrix}. \tag{27}$$

It can be shown that the FIM for the above parameters is equal to just the inverse of the covariance matrix.

$$\mathbf{F} = \mathbf{C}^{-1} = \begin{bmatrix} \frac{-1}{\sigma^2(\rho-1)} & \frac{\rho}{\sigma^2(\rho-1)} \\ \frac{\rho}{\sigma^2(\rho-1)} & \frac{-1}{\sigma^2(\rho-1)} \end{bmatrix} \quad . \tag{28}$$

Now, assume that a support constraint is applied such that the θ_1 is within the support and θ_2 is outside. By applying this support, we are affirming that the signal on θ_2 is zero. The support is applied to the FIM by zeroing out row two and column two. The resulting FIM is given by

$$\mathbf{F_s} = \begin{bmatrix} \dfrac{-1}{\sigma^2(\rho-1)} & 0 \\ 0 & 0 \end{bmatrix} . \tag{29}$$

In order to calculate the CRB of this element, the pseudo-inverse of the FIM is taken by inverting only the non-zero sub-matrix. In this case, only the element at (1,1) is inverted to give

$$\mathbf{F_s}^{-1} = \begin{bmatrix} -\sigma^2(\rho-1) & 0 \\ 0 & 0 \end{bmatrix} . \tag{30}$$

Therefore, the CRB of θ_1 is given by

$$CRB(\theta_1) = -\sigma^2(\rho-1) = \sigma^2(1-\rho) . \tag{31}$$

It is now evident that if the two pixels were perfectly correlated then CRB for θ_1 would be zero. If the two pixels were completely uncorrelated then the CRB for θ_1 would be the original read-noise variance. The same analysis can be extended to include all the parameters of the object and PSF.

3. IMAGE RECONSTRUCTION PARAMETERS

This chapter is dedicated to presenting and explaining all the parameters used in the calculations of the CRBs in the thesis. Two different objects are used for the CRB calculations and are explained first. Also, two different point-spread functions are used. These PSFs are explained next. This is followed by a discussion of the support constraints used for both objects and PSFs. Finally, the specifics of the noise model are given.

3.1. Object

Two objects were used in the research for this thesis. The first object was used in order to compare results with previous work in [7]. The object is a Russian satellite named OCNR5 shown below.

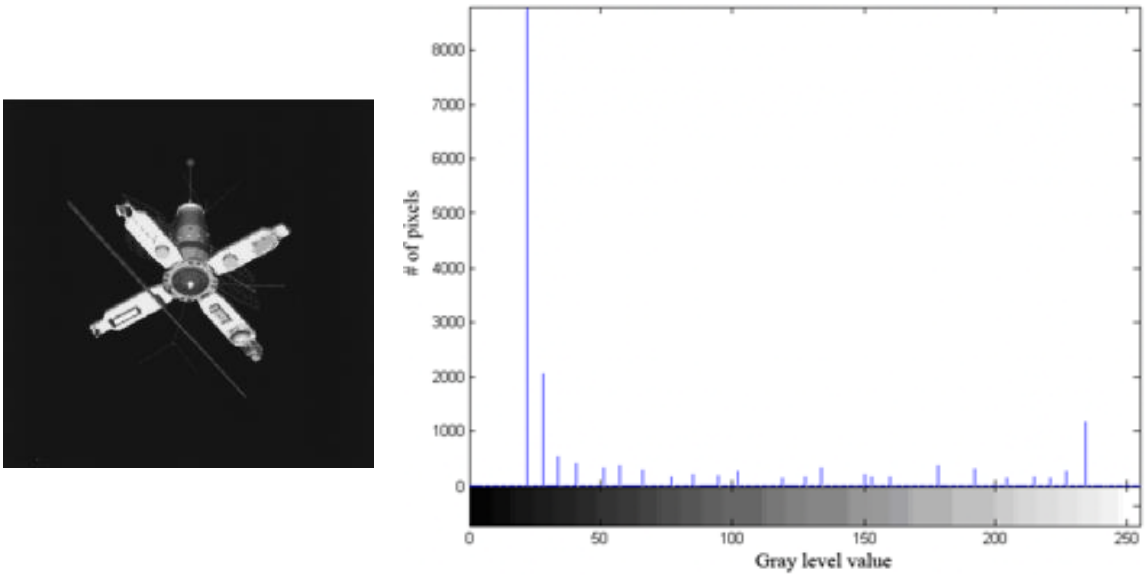

(a) (b)

Figure 2. (a) OCNR Satellite. (b) Histogram of (a)

Figure 2 is an image of the OCNR object and its histogram. From the histogram it is shown that the image has a good dynamic range. The full range of gray levels is represented, meaning that parts of the object have very high intensity values and other parts have low intensity values. The intensities in the object represent those of an object used in a real-world application. This object will be referred to as "OCNR".

Another object was also created and used in the CRB calculations to better understand certain trends in the CRB morphologies. The object simply consists of two circles of different intensities and radii with centers aligned on the x-axis. This object is shown below.

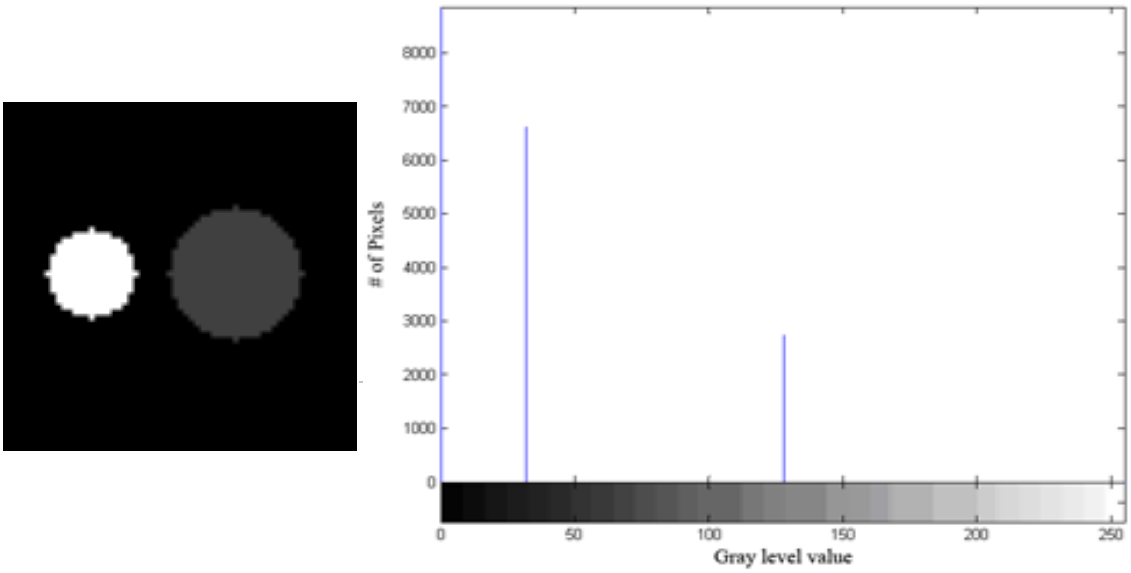

(a) (b)

Figure 3. (a) "twocirc" object. (b) Histogram of (a)

From the histogram above it is shown that only three intensity levels are present in the object. These represent the background (intensity = 0), the larger circle (intensity = 32) and the smaller circle (intensity = 128) respectively. Note, the image in Figure 3 is scaled so that both circles are visible. This object will be referred to as "twocirc."

The above objects are both digitized and stored in 64x64 arrays so that CRB computation-time is manageable.

3.2. Point Spread Function

The PSFs used to blur the object data are described in this section. Two sets of PSFs were used in the calculation of the CRBs. The first set was created by modeling real atmospheric characteristics. The second set was produced by specifying simple

geometrical cross-sections of the PSFs. Both PSF sets are explained in further detail in this section.

The first PSF set was modeled by considering a single point imaged through the atmosphere. The parameters used to describe the imaging system are based on the ratio of D / r_0 , where D is the imaging aperture diameter, and r_0 is the Fried seeing parameter. The Fried parameter is a measure of the effective diffraction-limited resolution of an aperture that is affected by the turbulent atmosphere [19]. In the case of this research, the D / r_0 ratio used was 8. These PSFs were created by specifying random coefficients for the Zernike parameters that correspond with the above D, r_0 [20]. 100 different PSFs were created in this manner. In order to have a concept of a perfect support region required by the discussion in Section 2.3.2, a support constraint that consists of a circle with radius 10 pixels was applied. This means that the circle was placed in the middle of the PSF array and any values outside the circle were set to 0. The first two PSF frames from this set along with their Fourier transforms are shown in Figure 4 and Figure 5.

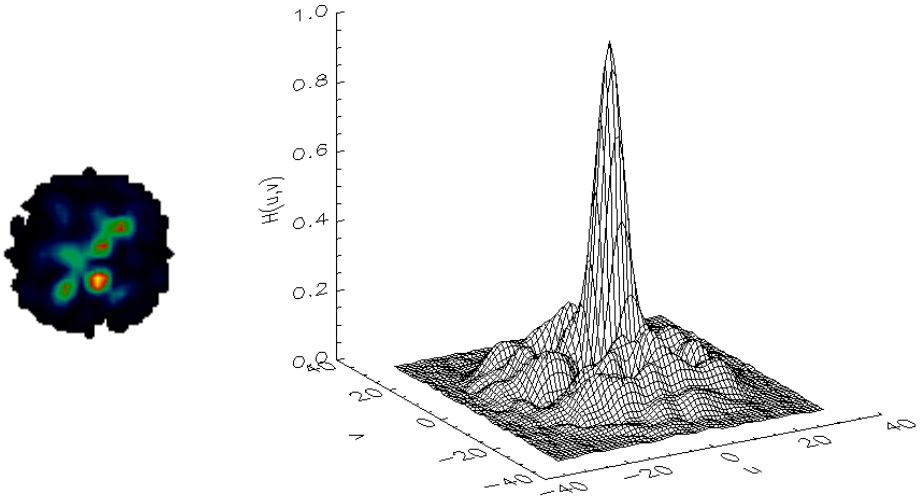

(a) (b)

Figure 4. (a) First frame of "atm" PSF set. (b) Fourier Transform of (a).

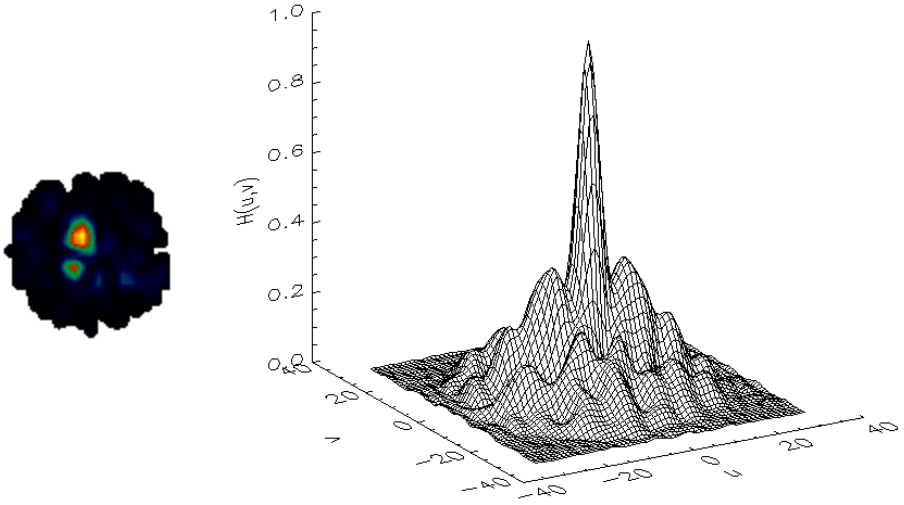

(a) (b)

Figure 5. (a) Second frame of "atm" PSF set. (b) Fourier transform of (b).

The PSFs in Figure 4 (a) and Figure 5 (a) have varying intensities within the support and thus, are not considered to be smooth. Furthermore, the PSFs from frame to frame are not

correlated and appear different from one another. These PSFs will be referred to as “atm” (for atmospheric) PSFs.

Enforcing the circle support also remedies another problem with the original PSF frames. Without the circle support, the PSFs are generally non-invertible in the Fourier domain. Applying the circle support in the spatial domain is equivalent to convolving the Fourier transform of the original PSF with the Fourier transform of the circle. This is shown in the following equation:

$$
\begin{aligned}
&h'(\vec{x}) = h(\vec{x})\, circ(\vec{x}) \quad , \\
&F\{h'\} = H(\vec{f}) * F\{circ\} \quad , \\
&\textit{where,} \\
&\quad circ(\vec{x}) = \begin{Bmatrix} 1, & |\vec{x}| \le a \\ 0, & elsewhere \end{Bmatrix} \quad , \\
&\quad F\{circ\} = \frac{J_1(\pi |\vec{f}|)}{2|\vec{f}|} \quad ,
\end{aligned}
\tag{32}
$$

$\mathcal{F}\{\ \}$ represents the Fourier transform, * represents convolution, h is the original PSF, H is the OTF and J_1 is a Bessel function of the first kind with order = 1. Thus, this convolution ensures that the OTF is invertible.

The second set of PSFs was designed to be smooth and have a small, predictable change from frame to frame. The contrasting nature of these PSFs and the above PSFs allows for a comparison of the effects of the PSF on the CRB calculations. Cross-sections of all 10 frames of the PSF set are shown in Figure 6.

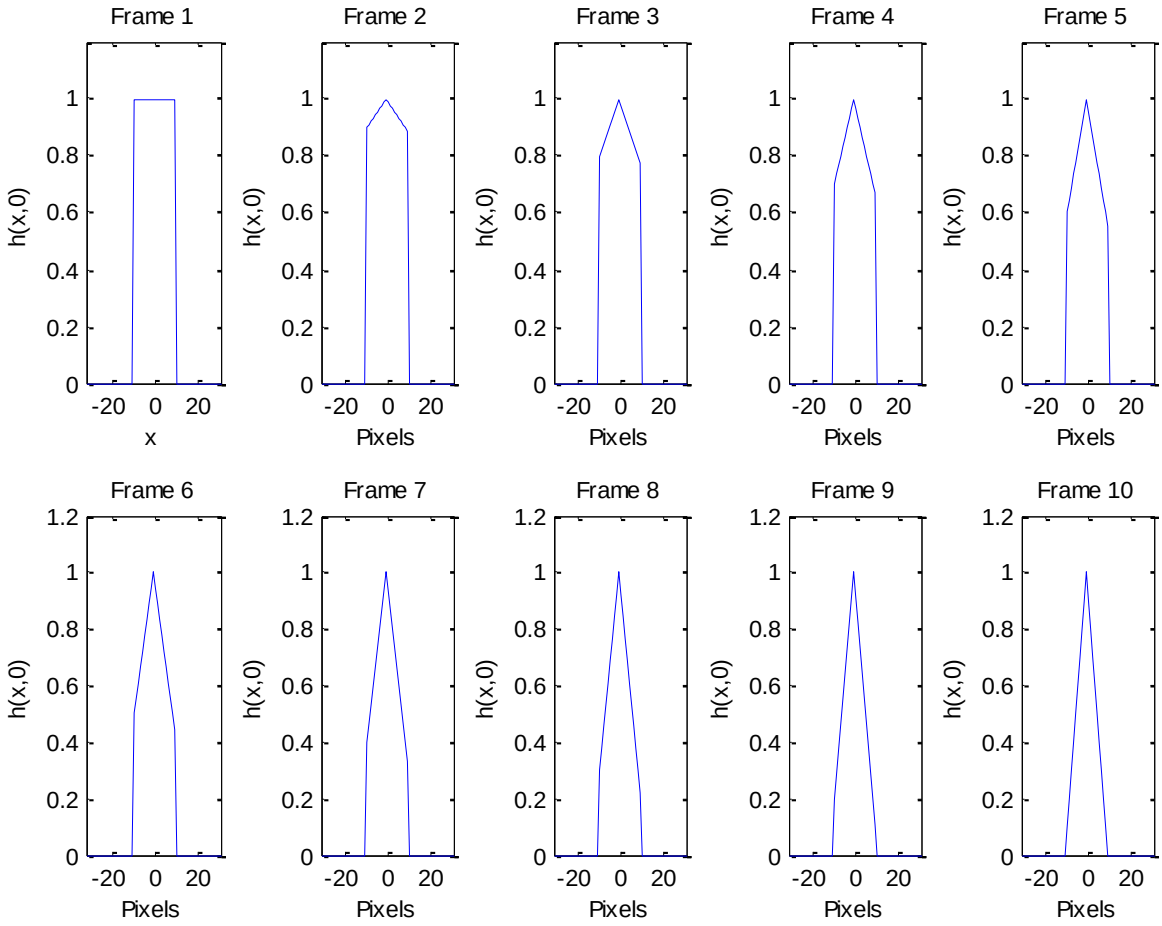

Figure 6. Horizontal slices through the centers of the 10 "rect2tri" PSF frames.

The first frame consists of ones inside the support and zeros outside. Each consecutive frame is a plateau of decreasing height capped with a triangle. These PSFs will be known as “rect2tri” PSFs. Note that while the cross-sections of the PSFs have a height of 1, this was only true for the creation of the PSFs. During the calculation of the CRBs, the PSFs are normalized to a total area of 1.

3.3. Support Regions

Support regions for both the objects and PSFs are needed in the CRB calculations. These support constraints define the area in which there is no signal outside the support. The tightest support for the two objects, called perfect support, is a binary image that encapsulates all the locations where the intensities are non-zero. The non-perfect supports are then generated by convolving the perfect support with different sized squares. This convolution effectively adds extra pixels to the edges of the perfect support region. These blurred support regions always encapsulate at least the pixels that contain the true object pixels. The supports used for the two objects are shown in the Figure 7.

(a) (b) (c)

Figure 7. Object supports for the OCNR object. (a) Perfect support region for OCNR. (b) Perfect support region convolved with a 2x2 square, known as Blur2. (c) Perfect support region convolved with a 7x7 square, known as Blur7. The support regions in (a), (b), and (c) contain 605, 805, and 1476 pixels, respectively.

(a) (b) (c)

Figure 8. Object supports for the "twocirc" object. (a) Perfect support region for the "twocirc" object. (b) Perfect support region convolved with a 2x2 square, known as Blur2. (c) Perfect support region convolved with a 7x7 square, known as Blur7. The support regions in (a), (b), and (c) contain 638, 724, and 1207 pixels, respectively.

As shown in Figure 7 and Figure 8, the support regions include an increasing number of pixels. In the reconstruction process these extra pixels must also be estimated. This increases the time it takes to reconstruct the image and also takes away from information that can be used during the reconstruction. Thus, it is always advantageous to define the tightest support region (the region that includes the object and the least number of pixels around it).

Since both sets of PSFs are contained entirely within a circle with a radius of 10 pixels, PSF supports can also be defined. The same set of supports is used for both the "atm" and "rect2tri" PSFs and consists of circles of varying radii. The perfect support in this case is just a circle with a radius of 10 pixels. The PSF supports used in the research are shown below.

(a) (b) (c)

Figure 9. PSF supports. (a) Perfect support, circle of radius 10. (b) Circle of radius 11. (c) Circle of radius 20. The support regions in (a), (b), and (c) contain 317, 377 and 1257 pixels, respectively.

3.4. Read Noise Characteristics

The read noise model is characterized well by a Gaussian distribution. For all the CRB calculations, read noise is always included. As explained in the previous chapter, the mean of the distribution is zero. A variance of 100 was chosen since this is a typical value for CCD cameras. The PDF for the noise model is given in the equation:

$$P(n;0) = \frac{1}{100\sqrt{2\pi}} \exp\left[-\frac{1}{2}\left(\frac{n}{100} \right)^2 \right] \quad , \tag{33}$$

where P is the PDF of the read noise.

4. COMPARISON TO NON-BLIND DECONVOLUTION

In this chapter, the results from previous work in [7] on non-blind deconvolution will be compared and contrasted to the results obtained from MFBD. It will be shown that the CRBs of the object estimate from MFBD will always be higher than the CRBs from non-blind deconvolution. The magnitude of this increase of CRBs is dependent upon the PSFs. Also, the morphology of the blind deconvolution CRBs differ from non-blind CRBs.

Although the results in [7] cover a range of imaging situations from simple to realistic, the results in this thesis are based on the simplest situation. This situation is characterized by the inclusion of only a read noise model and no regularization. Also, as mentioned in the background chapter, the previous work on non-blind deconvolution compared the CRBs obtained from using different support constraints to the CRBs obtained without using a support constraint. For the research in the thesis, different support regions will be compared to each other and compared to respective non-blind CRBs. The CRBs for the three object support regions described in Chapter 3 will be analyzed in two ways. First, the sum of the CRBs for each support region will be

compared in order to gain an overall understanding. Second, the morphology of those CRBs across the support region will be analyzed.

4.1. Sum of the CRBs

In this section, the sum of the blind deconvolution CRBs is compared to the sum of the non-blind deconvolution CRBs for various supports. The sums are calculated by totaling the CRBs over the entire support region. The CRBs using the OCNR object and the "rect2tri" PSF, for both blind and non-blind deconvolution are presented first. Table 1 contains the sums of the CRBs for both the non-blind and blind cases as functions of the size of the support constraint. The last column is a ratio of the sum of the CRBs for blind deconvolution to the sum of the CRBs for non-blind deconvolution.

Object Support	Non Blind	Blind	Ratio
Perfect	4.96E+08	6.68E+08	1.35
Blur2	7.55E+08	1.01E+09	1.34
Blur7	1.86E+09	2.42E+09	1.30

Table 1. Sum of the CRBs for both non-blind and blind cases using the OCNR object and the "rect2tri" PSF set..

Two observations can be made from the data in the above table. First, as the size of the support region is increased, the CRBs for both non-blind and blind deconvolution increase. This is expected since the larger support constraints have larger areas in which the CRBs are summed over. However, not only does the size of the support contribute to the increase, the CRBs at each pixel are also higher. Second, the sum of the blind deconvolution CRBs is a factor of about 35% higher than non-blind CRBs for the case of perfect support and a factor of only 30% higher for the case of Blur7 support. This

indicates that the sum of the blind deconvolution CRBs increases less than the sum of the non-blind CRBs as the support is increased. This phenomenon is not due to MFBD itself, but rather, is caused by properties of the PSF. This is evident in Table 2, which contains the sums of the CRBs from non-blind and blind deconvolution using the OCNR object and the "atm" PSF.

Object Support	Non Blind	Blind	Ratio (Blind/Non)
Perfect	1.13E+09	1.59E+09	1.41
Blur2	1.96E+09	2.86E+09	1.46
Blur7	6.18E+09	1.19E+10	1.93

Table 2. . Sum of the CRBs for both non-blind and blind cases using the OCNR object and the "atm" PSF set..

Two observations about the sum of the CRBs from the "atm" PSF set are made. First, similar to the case using the "rect2tri" PSF, the blind deconvolution CRBs are higher than the non-blind CRBs in each case. However, unlike with the "rect2tri" PSF, as the size of the object support is increased, the sum of the blind deconvolution CRBs increases more than the sum of the non-blind CRBs.

The comparison of CRBs using the "rect2tri" PSF with the CRBs using the "atm" PSF reveals two details. First, employing blind deconvolution over non-blind deconvolution always increases the object CRBs. Second, the specific PSF governs the magnitude of the increase. Research with other PSFs has yielded ratios of blind deconvolution CRBs to non-blind CRBs as low as 30% and as high as 200%. Although it is not known at this time which characteristics of the PSF cause this behavior, further insight can gained by considering the CRBs of the PSF estimates. Since blind

deconvolution also estimates the PSF, the CRBs of the PSF estimate can be calculated. Figure 10 shows a plot of the PSF CRBs.

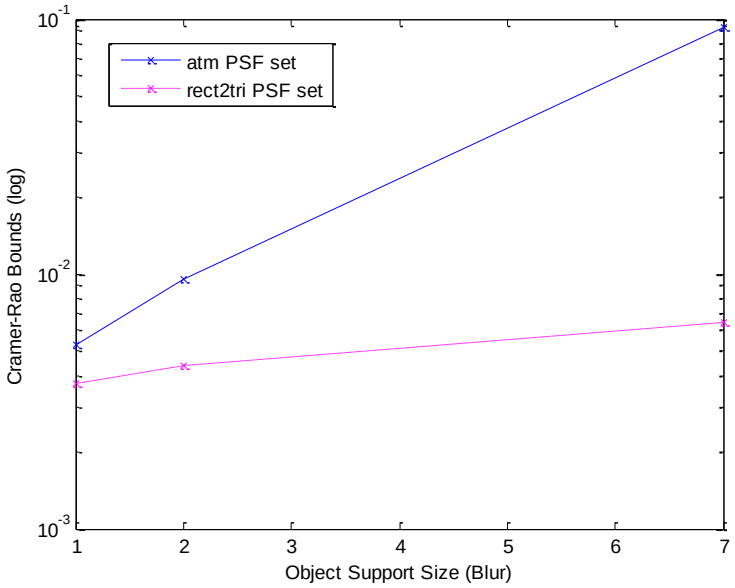

Figure 10. Plot of the CRBs of the point spread functions. The solid line corresponds to the "atm" PSF set and the dashed line corresponds to the "rect2tri" PSF set

It is shown in Figure 10 that the sum of the CRBs increases much more for the "atm" PSF than the "rect2tri" PSF. Although, in general, a strong correlation does not exist between the CRBs of the object and the CRBs of the PSF, in this case the increase in PSF CRBs for the "atm" gives insight into the increase of the object CRBs.

4.2. Morphology of the CRBs

To better understand how the support constraint impacts MFBD, the distributions of the CRBs across the support regions are analyzed. It is well understood that the correlations between intensities inside and outside the support contribute to the noise

reduction in the reconstruction [7]. Also, a simple example of this phenomenon is given in Section 2.3.3. Since the correlations are stronger for pixels closer together the most noise reduction takes place toward the edge of the support for the non-blind case. This is illustrated in Figure 11 for the case of perfect object support.

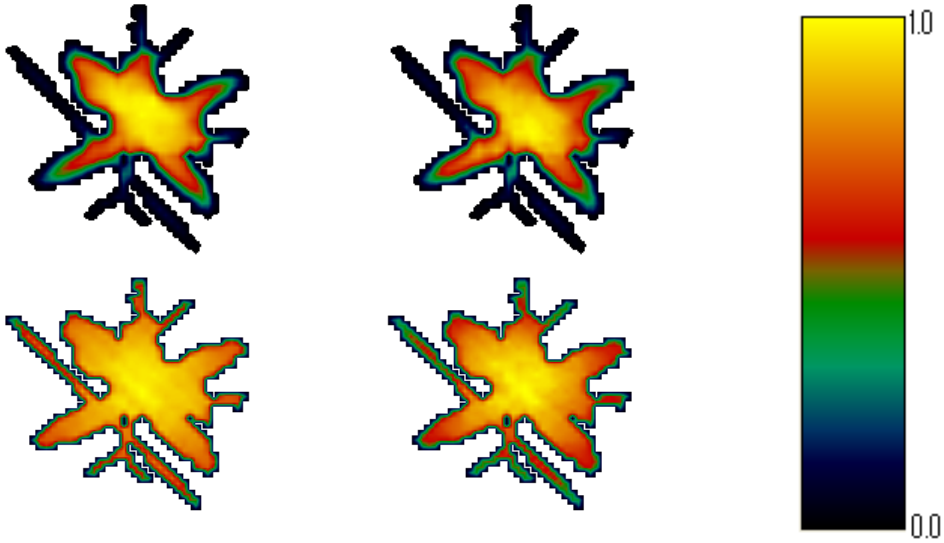

Figure 11. Morphologies of the CRBs for the following cases: (a) Non-Blind, "atm" PSF; (b) Blind, "atm" PSF; (c) Non-Blind, "rect2tri" PSF; (d) Non-Blind, "rect2tri" PSF; Blur1 object support is common to all the cases.

It is important to mention that each image is normalized to a maximum value of 1.0 before being displayed. Hence, only the regions of high CRBs and low CRBs can be compared within each image itself and the CRBs cannot be compared between images. From Figure 11 it is shown that in all the cases the CRBs are highest in the center and decrease toward the edges of the support. For both PSFs, the morphology of the blind deconvolution CRBs matches that of the non-blind CRBs. However, it is shown in the Figure 12 that this is not the case as the size of the object support is increased.

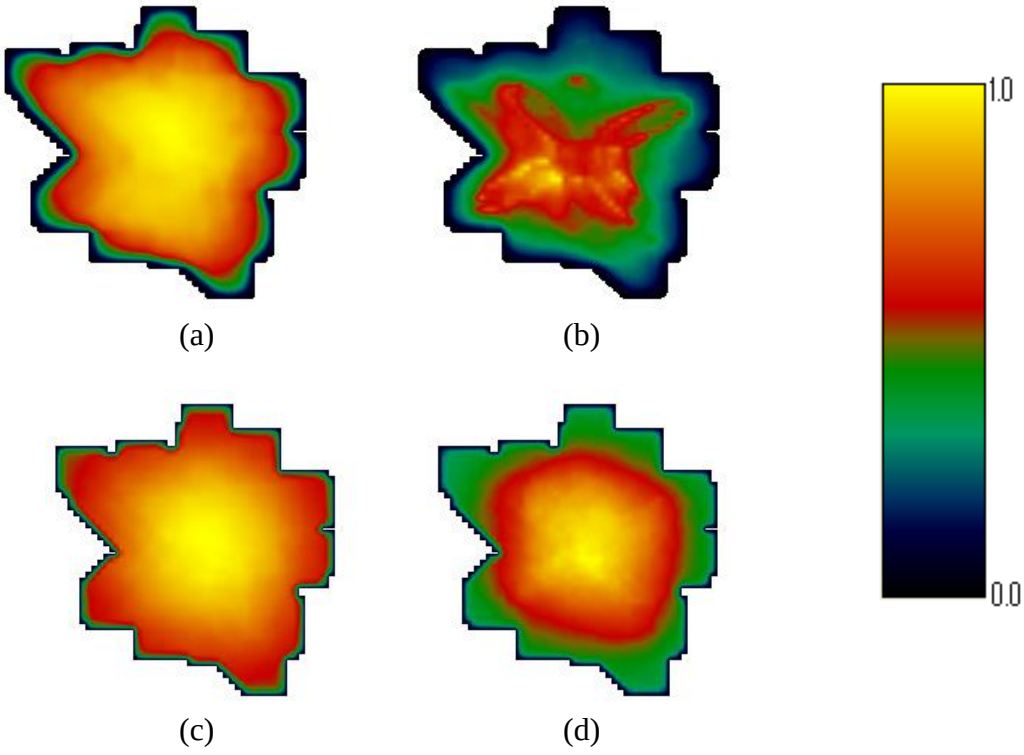

Figure 12. Morphologies of the CRBs for the following cases: (a) Non-Blind, "atm" PSF; (b) Blind, "atm" PSF; (c) Non-Blind, "rect2tri" PSF; (d) Non-Blind, "rect2tri" PSF; Blur7 object support is common to all the cases.

Figure 12 reveals the differences in morphologies of blind deconvolution CRBs to their non-blind counterparts. While generally the CRBs are still higher in the center and decrease toward the edges, two other observations can be made. First, it is shown that the blind deconvolution CRBs for both PSFs are clustered toward the true object support and are not solely a function of the distance to the edge of the applied support as in the non-blind case. Second, in Figure 12 (b), for the case of the "atm" PSF, it is shown that the increase in the ratio of blind deconvolution CRBs to non-blind CRBs from Table 1 is present on the edges of the object. These two observations are shown clearer in Figure 13.

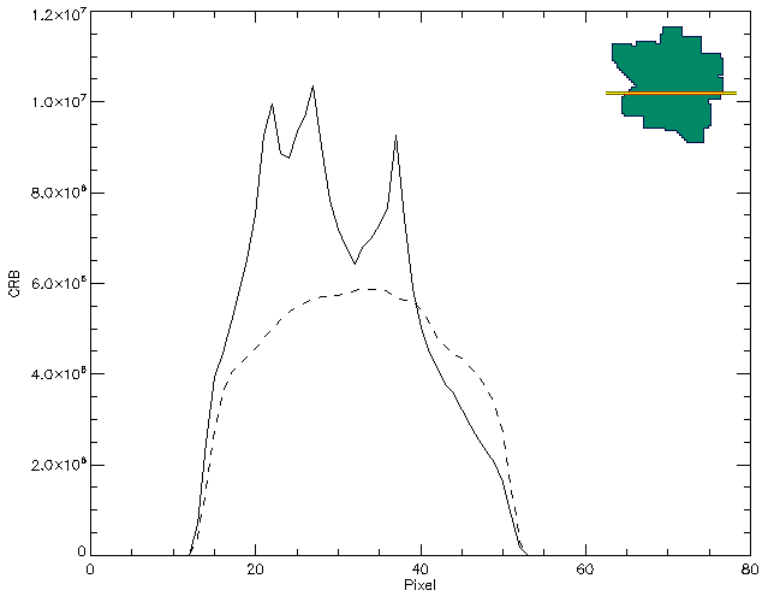

Figure 13. Slices of the blind deconvolution (solid line) and non-blind (dashed line) CRBs using the "atm" PSF set and Blur7 object support.

In Figure 13, the solid line represents the blind deconvolution CRBs and the dashed line represents the non-blind CRBs. The graphic in the upper right-hand corner depicts the position of the slice through the support. In order to display both blind and non-blind slices on the same axis, the blind deconvolution CRBs were normalized to the total of the non-blind CRBs. Notice that the solid line has three distinctive peaks. The first two are centered on pixel location 25 and correspond to the wing of the object that points in the southwest direction. The second peak is centered on pixel location 40 and corresponds to the wing that points in the southeast direction. Also, notice that the blind deconvolution CRBs are clustered into a smaller region than the non-blind CRBs.

In order to gain further insight into how the actual object affects the morphologies of the CRBs, the "twocirc" object is used in the CRB calculations. The relatively simple makeup of this object permits a clearer understanding of the differences in morphologies

of blind and non-blind deconvolution. First, the morphologies of the CRBs, for both blind and non-blind deconvolution, using both the PSFs and a perfect object support constraint are displayed in Figure 14.

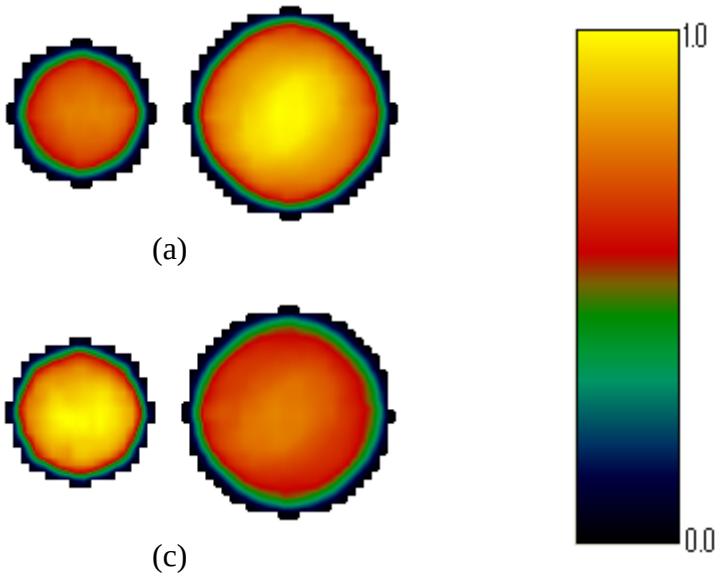

(a)

(c)

Figure 14. Morphologies of the CRBs for the following cases: (a) Non-Blind, "atm" PSF; (b) Blind, "atm" PSF; Blur1 object support is common to all the cases.

Using the "twocirc" object, it is shown that even with the perfect object support, there is exists a dissimilarity between the morphologies of the blind deconvolution CRBs and the non-blind CRBs. Figure 14 (a) shows the morphology of the non-blind CRBs. It is evident that the CRBs are solely a function of the distance from the edge of the support. The CRBs are higher in the center of the larger circle than the in center of the smaller circle. However, this is not the case for Figure 14 (b). Using the Blur7 support shows same phenomena.

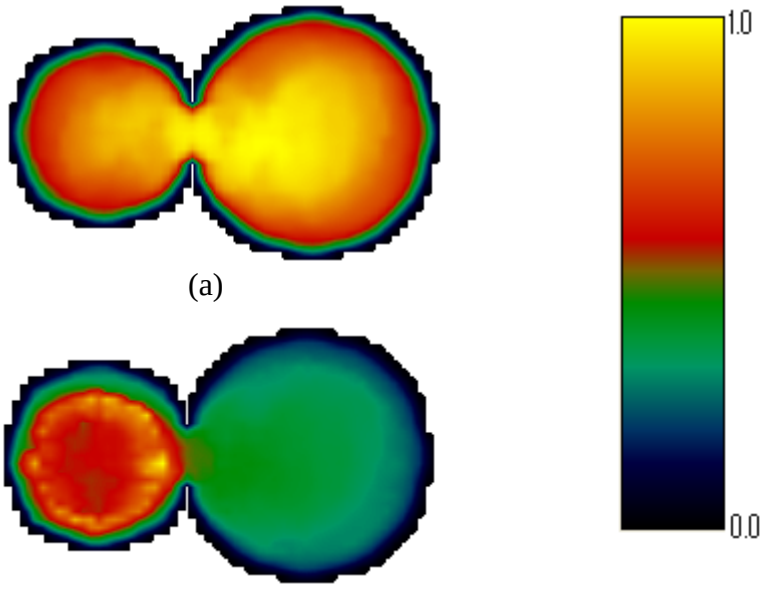

(a)

(b)

Figure 15. Morphologies of the CRBs for the following cases: (a) Non-Blind, "atm" PSF; (b) Blind, "atm" PSF; Blur7 object support is common to all the cases.

Figure 15 shows the morphologies of both the blind deconvolution CRBs and non-blind CRBs using the Blur7 support. Again, it is shown from the non-blind case that the morphology is a function of the distance from the edges of the support. However, for the blind deconvolution CRBs, this is not true. In the smaller circle, it is shown that the CRBs are clustered toward the perfect object support and the CRBs are higher at the edge of that circle. The morphology of blind deconvolution CRBs does not match the morphology of non-blind CRBs and further research needs to be conducted in order to understand the cause of this discrepancy.

5. ANALYSIS OF MULTI-FRAME BLIND DECONVOLUTION PARAMETERS

The results presented in this chapter focus on the effects on MFBD from parameters that were not explored in previous work in [7]. Particularly, two of these parameters will be considered. First, the size of the PSF support is varied. Second, multiple measurement frames will be included in the reconstruction process. The effects on the CRBs from these parameters will be analyzed. It is shown that adding multiple measurement frames always decreases the sum of the CRBs. In particular, the decrease is greatest for the first few frames. Properties of the actual PSFs play a dominant role in how much the sums of the CRBs actually decrease. It is also shown that as the size of PSF support is increased, the sums of the CRBs also increase. The increase, however, is minor when considering the increase in CRBs as a result of increasing the size of the object support.

5.1. PSF support

In this section the effects on the CRBs of the object as a function of the size of the PSF support are analyzed. These CRBs are calculated using the three PSF support

constraints described in Chapter 3. It is shown that increasing the PSF support does not have a significant impact on the object CRBs. The sums of the CRBs as a function of the PSF support are calculated for both the "atm" and "rect2tri" PSFs. For comparison purposes, the tables that contain the sums of the CRBs as a function of the object support are also shown.

PSF Support	Number of Pixels in the Support	Blind Deconvolution CRBs
Circle, radius 10	316	6.68E+08
Circle, radius 11	376	7.51E+08
Circle, radius 20	1256	1.70E+09

Table 3. Blind deconvolution CRBs as a function of the PSF support. The CRBs are calculated using the OCNR object and "rect2tri" PSF.

Object Support	Number of Pixels in the Support	Blind Deconvolution CRBs
Perfect	604	6.68E+08
Blur2	804	1.01E+09
Blur7	1476	2.42E+09

Table 4. Blind deconvolution CRBs as a function of the object support. The CRBs are calculated using the OCNR object and "rect2tri" PSF.

First, the "rect2tri" PSF is considered. Tables 3 and 4 contain the sum of the CRBs using the OCNR object and the "rect2tri" PSF as a result of increasing the size of the PSF support and increasing the size of the object support, respectively. The tables also contain the number of pixels in each of the supports. There are 4 times as many pixels in the largest PSF support compared to the smallest PSF support. Of the object supports used, there are 2 times as many pixels in the largest object support than the smallest object support. The difference in the sums of the CRBs between the largest PSF support and smallest PSF support is approximately a factor of 2.5. However, the

difference in the sums of the CRBs between the largest object support and smallest object support is a factor of almost 4. As the smoothness properties of the PSF degenerate, this separation worsens.

PSF Support	Number of Pixels in the Support	Blind Deconvolution CRBs
Circle, radius 10	316	1.59E+09
Circle, radius 11	376	1.71E+09
Circle, radius 20	1256	3.39E+09

Table 5. Blind deconvolution CRBs as a function of the PSF support. The CRBs are calculated using the OCNR object and "atm" PSF.

Object Support	Number of Pixels in the Support	Blind Deconvolution CRBs
Perfect	604	1.59E+09
Blur2	804	2.86E+09
Blur7	1476	1.19E+10

Table 6. Blind deconvolution CRBs as a function of the object support. The CRBs are calculated using the OCNR object and "atm" PSF.

Tables 4 and 5 contain the sum of the CRBs using the OCNR object and the "atm" PSF as a result of increasing the size of the PSF support and increasing the size of the object support, respectively. Using the largest PSF support compared to the smallest increases the object CRBs by a factor of only 2. Conversely, using the larger object support compared to the smallest increases the object CRBs by a factor of almost 7! Although the actual numbers are dependent on the specific PSF used, they are indicative of the impact of the size of object support compared to the size of the PSF support using

any arbitrary PSF. Therefore, efforts should be concentrated on finding the tightest object support possible.

Furthermore, it is shown that increasing the size of the PSF support does not change the morphology of the CRBs. From Chapter 4, recall that increasing the size of the object support caused the morphologies to change for the blind deconvolution CRBs. This was especially apparent for the "atm" PSF, where CRBs increased the most at the edges of the object. Conversely, this is not true when the PSF support is increased. Figure 16 contains images of the morphologies of the CRBs for the "atm" PSF as a function of the PSF support.

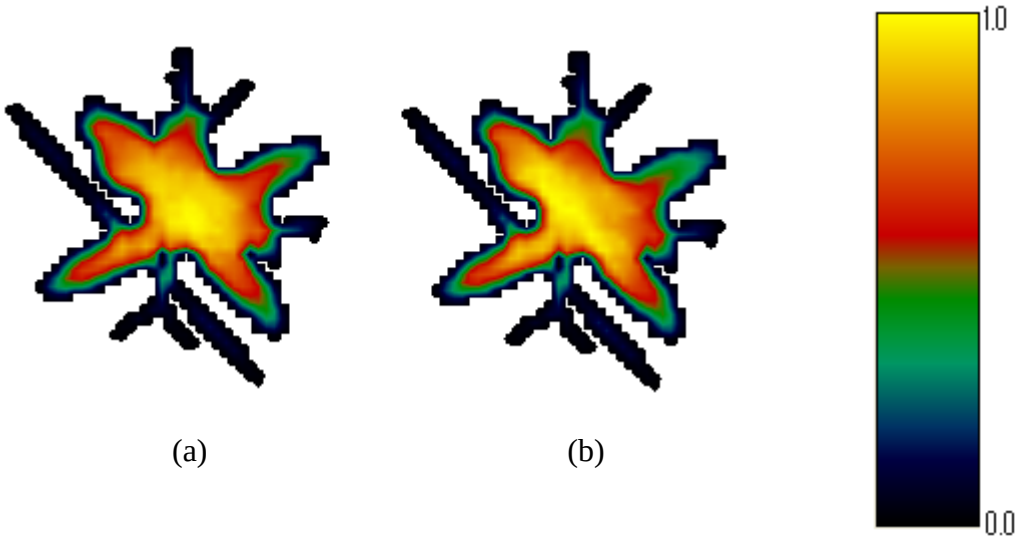

(a) (b)

Figure 16. Morphologies of the CRBs using the "atm" PSF. (a) corresponds to a circle PSF support of radius 10; (b) corresponds to a circle PSF support of radius 20

5.2. Multiple Frames

In this section, the CRBs of the object are analyzed as a function of including multiple measurement frames. Including multiple measurement frames is not unique to MFBD as they can also be incorporated into non-blind deconvolution estimations. However, multiple frames were not considered in [7]. Therefore, the results are presented in this chapter rather than the previous. Non-blind CRBs are calculated along with blind deconvolution CRBs and the results are compared in this section. First, using the same PSF multiple times, with differing noise realizations is considered. For both the non-blind and blind deconvolution cases, the decreases in the sums of the CRBs follow a simple mathematical model. Next, different PSF functions are used and it is shown that the different PSF frames produce different CRBs. Also, the benefit from using just one additional frame is studied in detail as a function of the object support.

Including multiple measurement frames always decreases the sum of the CRBs. This decrease in CRBs can be modeled from probability theory [21]. Consider two random variables that are independent and uncorrelated, X_1 and X_2, each parameterized by the same mean, μ, and variance, σ^2. Summing these two variables and dividing by two produces a new a random variable, Y. Now, consider extending this example to N random variables, each parameterized by the same mean, μ, and variance, σ^2. Again, Y is the sum of these N variables divided by N. The variance of Y is given by the following equations:

$$
\begin{aligned}
&Y = \frac{1}{N}\sum_{i=1}^{N} X_i \,;\; \mathrm{var}\{X_i\} = \sigma^2 \quad , \\
&\mathrm{var}\{Y\} = \mathrm{var}\left\{\frac{1}{N}\sum_{i=1}^{N} X_i\right\} = \left(\frac{1}{N}\right)^2 \sum_{i=1}^{N} \mathrm{var}\{X_i\} \\
&\qquad = \left(\frac{1}{N}\right)^2 N\sigma^2 = \frac{\sigma^2}{N} \quad ,
\end{aligned}
\tag{34}
$$

where X_i represents a random variable with mean, μ, and variance, σ^2 in the equations above. Thus, the equations above give the variance for the average of N independent, identically distributed random variables. In order to apply this concept to multiple blurred and noisy measurement frames, the frames must also by identically distributed and independent. To show that the frames are identically distributed two notions are considered. First, each pixel in each measurement frame is a random variable. The mean of a pixel is given as a function of the convolution of the PSF and the object at that pixel. The variance is equal to the variance of the zero-mean noise model discussed in Chapter 3. Second, each X_i in the equation above represents the sum of the pixels in each frame of the object reconstruction. Therefore, X_i is also random variable. The mean of X_i is given by summing the means of each pixel. However, the pixels in any given frame are not necessarily spatially uncorrelated and therefore, not independent. Consequently, the variance of X_i is not just the sum of the variances of each pixel, but is a function of the how a specific PSF spatially correlates the noise of the pixels. Therefore, only by using the same PSF are the X_i 's identically distributed. Even when the same PSF is used, the noise realizations of the two frames are different. As a result, using the same PSF, the random variable given by the sum of the pixels in one measurement frame is identically distributed and independent from the random variable given by the sum of the pixels in another measurement frame. This satisfies the criteria for the model in Eq. (34).

From the discussion above, it is shown that averaging multiple measurement frames should produce CRBs that decrease as *1/N*, where *N* is the number of included frames. MFBD CRBs were calculated using the same PSF frame 10 times. Figure 17 shows the CRBs plotted along with the *1/N* curve normalized to the sum of the CRBs of the first frame.

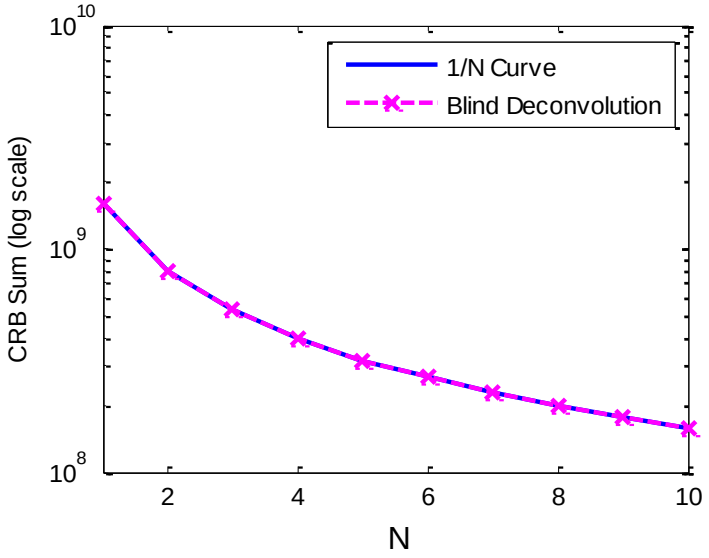

Figure 17. Plot of the sum of the blind deconvolution CRBs and *1/N* curve normalized to the sum of the first frame of the blind deconvolution CRBs. The same PSF frame was used for all 10 frames.

Indeed, the sums of the MFBD CRBs follow the *1/N* curve. The exact match to the *1/N* is true regardless of the actual PSF function. The same is also true for non-blind deconvolution CRBs.

It is well known that when imaging through the atmosphere, such as with the case of speckle imaging, including *N* measurement frames increases the signal-to-noise ratio (SNR) by a factor of the square root of the *N* [22]. The SNR is calculated by dividing the

mean of a frame by the square root of the variance. Thus, an increase by a factor of $\sqrt{N}$ in the SNR corresponds to a decrease by a factor of N in the CRBs of blind deconvolution. Since blind deconvolution is a comparable algorithm to speckle imaging [23], it is expected that the sum of the CRBs from including N measurement frames decreases according to the *1/N* model. However, the results below show that this is not the case when only a few frames are included.

10 different PSFs are now used in the CRB calculations. Figure 18 (a) is a plot of the sum of the CRBs using the first 10 frames in the "atm" PSF set, along with the normalized *1/N* curve. Figure 18 (b) is a plot of the sum of the CRBs using the 10 frames in the "rect2tri" PSF set, along with the normalized *1/N* curve.

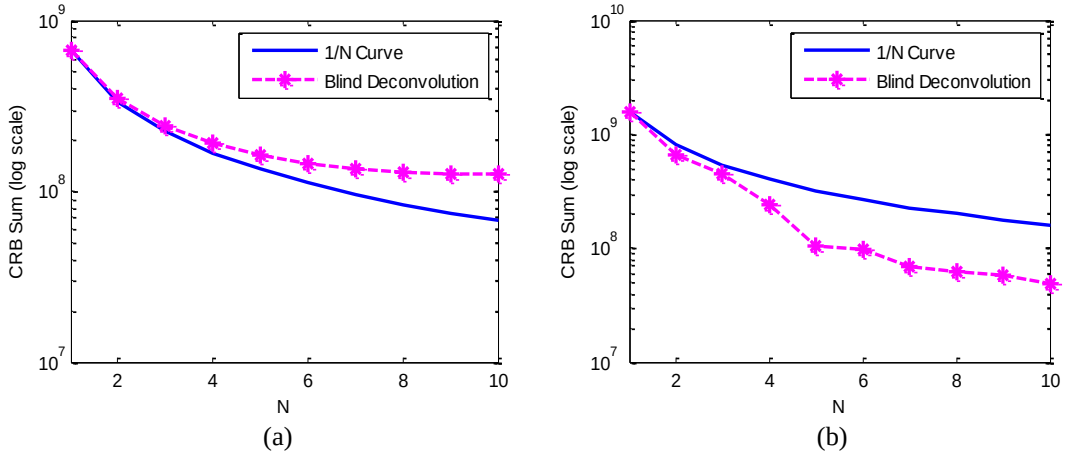

Figure 18. Plot of the sum of the blind deconvolution CRBs and *1/N* curve normalized to the sum of the first frame of the blind deconvolution CRBs. The CRBs were calculated using the "atm" PSF set for (a) and the "rect2tri" PSF set for (b). Blur1 object support was common to both.

From the plots above it is clearly shown that the curves representing the blind deconvolution CRB sums do not follow the *1/N* curve exactly. By comparing the slope of

the sums of the CRBs between two adjacent frames to the slope of the *1/N* curve between the same two adjacent frames, the benefit of including a particular frame can be gauged. Using this metric and considering Figure 18 (b), it is shown that the most prevalent benefits are produced by the inclusion of frames 4 and 5. Frame 2 also provides a greater benefit than predicted by the model. This implies that a property specific to the 2^{nd}, 4^{th}, and 5^{th} frames of the "atm" PSF set lowers the CRBs more the *1/N* model predicts. Now, considering the plot in Figure 18 (a), it is shown that including the 2^{nd} frame produces CRBs that are higher than those predicted by the *1/N* model. Again, this implies that there is a property specific to the 2^{nd} frame of the "rect2tri" PSF set that produces higher CRBs. In order to verify that specific PSF frames cause this non-predictive behavior, the same 10 frames used for the blind deconvolution CRB calculations in Figure 18 (b) are used in non-blind CRB calculations. A plot of the sum of the CRBs as a result of including each frame is plotted in Figure 19 along with the normalized *1/N* curve. It is shown that the same specific PSF frames cause the behaviors.

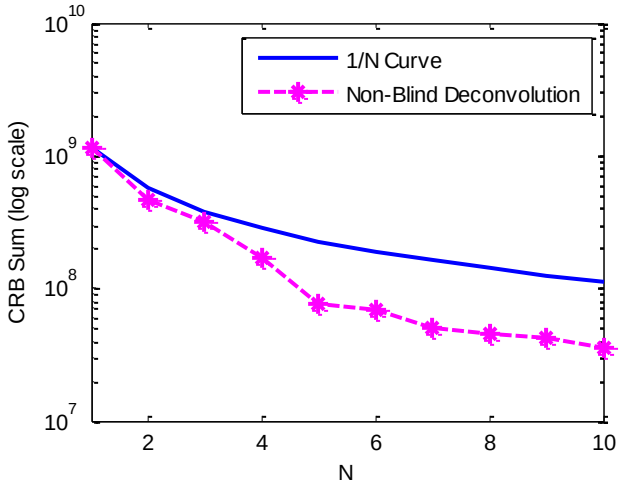

Figure 19. Plot of the sum of the non-blind deconvolution CRBs and *1/N* curve normalized to the sum of the first frame of the non-blind deconvolution CRBs. The OCNR object and "atm" PSF was used in the CRB calculations.

It is shown in Figure 19 that specific frames cause the CRBs to deviate from the *1/N* curve. Particularly, in Figure 18 (b), the inclusion of frames 2, 4 and 5 cause the most significant deviations. However, the order in which the frames are included also contributes to the deviations. By using the same 10 frames and simply reversing the order, such that the 10^{th} frame is used first, the 9^{th} frame second, etc. it is shown that the same frames do not cause the CRBs to deviate when included in a different order. Figure 20 shows the CRBs using the first 10 frames from the "atm" PSFs and the 10 frames from the "rect2tri" PSFs in the reverse order.

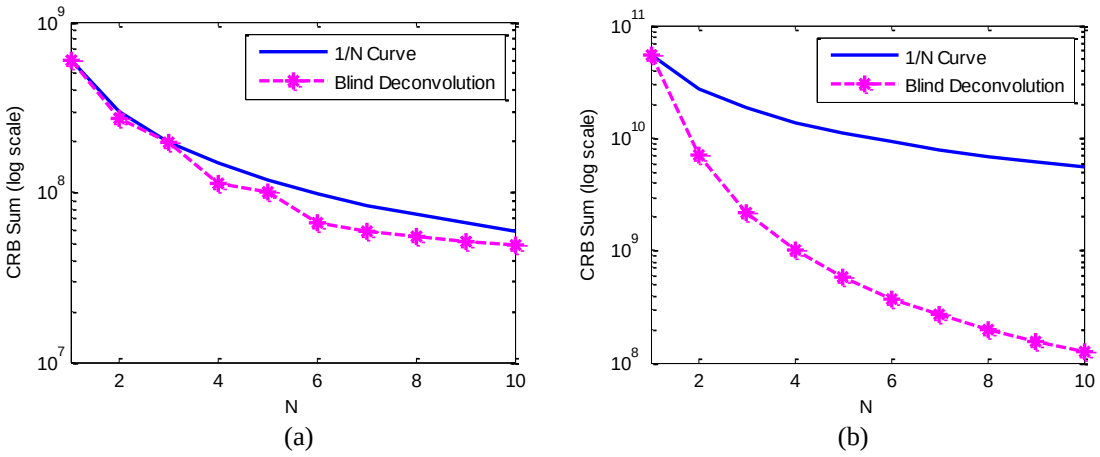

Figure 20. Plot of the sum of the blind deconvolution CRBs and *1/N* curve normalized to the sum of the first frame of the blind deconvolution CRBs. The CRBs were calculated using the first 10 frames of the "atm" PSF set in reverse order for (a) and the "rect2tri" PSFs in reverse order for (b). Blur1 object support was common to both.

It is evident from Figure 20 that the properties of specific PSF frames only cause deviations of the CRBs from the *1/N* curve for the first few frames. As more frames are added the specific properties have less of an impact on the CRBs. After including about 8 frames, the sum of the CRBs closely follow the *1/N* curve. This is shown in the plot in Figure 21, where 20 frames of the "atm" PSF set are used. Instead of normalizing the *1/N* curve to the sum of the CRBs in frame 1 as in the previous plots, the curve is normalized to frame 9. Therefore, the *1/N* curve matches the sum of the CRBs for frame 9. This normalization is performed to show that after frame 9 the CRBs match the *1/N* curve.

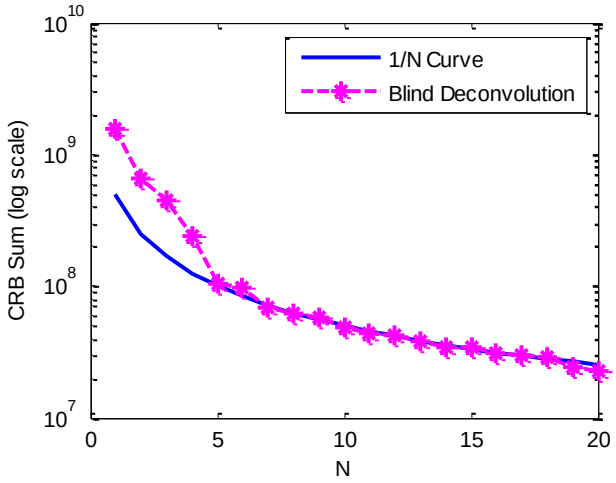

Figure 21. Plot of the sums of the CRBs calculated using the first 20 frames of the "atm" PSF set. The *1/N* curve is normalized to the 9th frame. The "atm" PSF set and Blur1 object support were used for the CRB calculations.

The individual characteristics of the PSFs have less of an impact on the deviation of the CRBs from the *1/N* curve as more frames are added because the properties of the PSFs are averaged out. This is shown for both PSF sets. First, a PSF set consisting of 20 frames was created by randomly selecting the frames from the "rect2tri" set. Next, these randomly selected 20 frames were averaged by adding all the frames and normalizing to a height of 1. Finally, the CRBs were calculated using the random PSF set and plotted with the CRBs calculated using the average PSF. The CRBs are shown in Figure 22. It is important to note that in Figure 22 the CRBs are not normalized. Thus, it is evident that the CRBs of the 20 frames closely match the CRBs of the average PSF with the inclusion of just 4 frames.

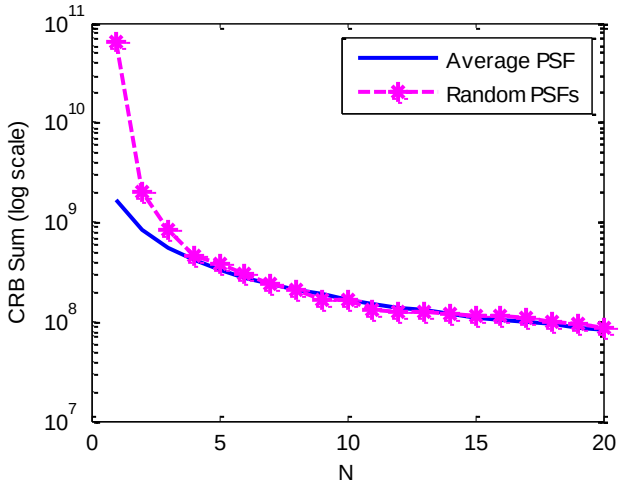

Figure 22. Plot of the CRBs of 20 randomly selected PSFs from the "rect2tri" set along with the CRBs of the average PSF.

Similarly, the average PSF of the first 20 frames from the "atm" PSF was created. The CRBs using the first 20 frames is plotted with the CRBs using the average PSF in Figure 23.

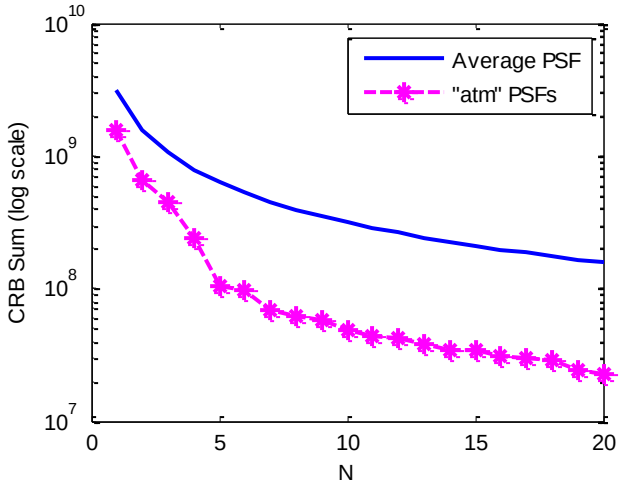

Figure 23. Plot of the CRBs of the first 20 "atm" PSFs along with the CRBs of the average PSF.

Although the CRBs using the "atm" PSFs do not match the CRBs of the average PSF, the slopes of the two match after frame 5. The discrepancy is caused by an inherent property of the "atm" PSF set. When averaging these PSFs, some high spatial frequency

information is lost. As a result, the CRBs of the average PSF are higher than the CRBs of the actual PSFs. This loss of high spatial frequency content is apparent when comparing the Fourier transform of the first "atm" PSF and the average of the 20 "atm" PSFs. These functions are displayed in the Figure 24.

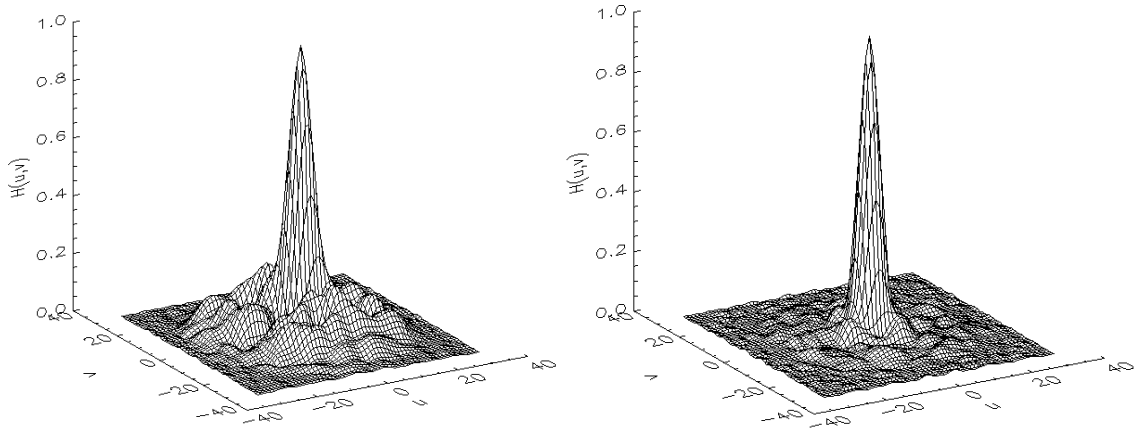

Figure 24. 3-D surface views of the OTFs corresponding to the first frame of the "atm" PSF set in (a) and the average of the first 20 frames in (b).

Conversely, averaging the 20 random frames chosen from the "rect2tri" set simply produces a PSF that resembles frame 5 of the "rect2tri" set. This is due to the fact that the original 10 "rect2tri" PSFs average to frame 5. By displaying the Fourier transform of frame 5 of the "rect2tri" set and the Fourier transform of the average of the 20 random frames, we see that no significant high spatial frequency information is lost.

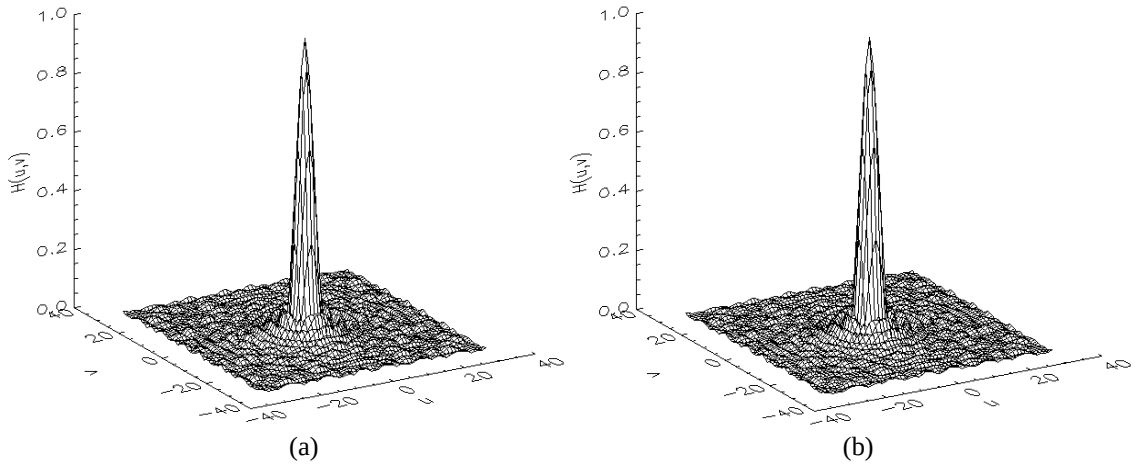

Figure 25. 3-D surface views of the OTFs corresponding to frame 5 of the "rect2tri" PSF set in (a) and the average of the 20 randomly selected frames from the "rect2tri" set in (b).

It is not understood at this time which properties of the PSF frames cause variations from the *1/N* model. However, further insight into this phenomenon is gained by considering the role of the support constraints. From Section 5.1 in this chapter, it is shown that the variations in the PSF support constraint have minor impact on the object CRBs. Therefore, only the object support constraint is considered here. Also, it is shown above that as more frames are added the CRBs begin to conform to the *1/N* curve. Thus, the specific properties of the PSF have the most potential to cause deviation from the *1/N* curve when applied to the 2nd frame. Therefore, the benefit of the 2nd frame as a function of the size of the object support is discussed here.

In order to quantify the benefit of including the 2nd frame, consider the slope of the CRBs between the first two frames to the slope of the *1/N* curve between the same two frames. The benefit of including the 2nd frame is quantified in the equation,

$$
\begin{aligned}
B &= \frac{\text{Actual Slope}}{\text{Expected Slope}} \\
&= \frac{CRB\{F_1\} - CRB\{F_2\}}{CRB\{F_1\} - \frac{CRB\{F_1\}}{2}} \\
&= 2\left(1 - \frac{CRB\{F_2\}}{CRB\{F_1\}}\right)
\end{aligned}, \tag{35}
$$

where $CRB\{F_i\}$ represents the sum of the CRBs of a specific frame, *i*. If including the 2nd frame reduces the sum of the CRBs exactly as the *1/N* model predicts, then the benefit, *B*, of including that frame is equal to one. If including the frame reduces the sum of the CRBs by more than *1/N*, then the benefit, *B*, is a number greater than 1. If including a frame reduces the sum of the CRBs by less than *1/N*, then the benefit, *B*, is a number less than one.

The benefit of including the 2nd frame was calculated using 50 different 2-frame sets picked from the "atm" PSF set. Perfect object support was used for these CRB calculations. The histogram in Figure 26 shows the benefits from these sets.

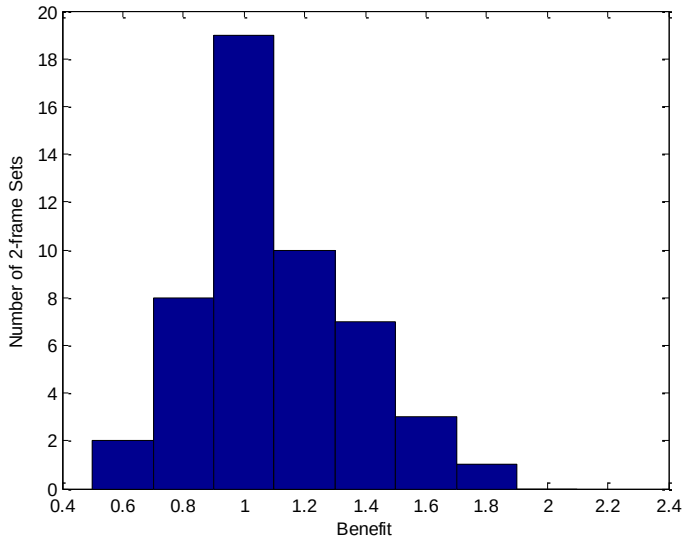

Figure 26. Histogram of the benefits calculated using 50 2-frame sets taken from the "atm" PSF set. Blur1 object support was used in the CRB calculations.

As shown in the histogram, the benefits are spread between .6 and 1.8. The average of these benefits is 1.07. By increasing the object support, the average benefit increases, but the shape of the histogram does not significantly change. This is evident from the plot in Figure 27 in which Blur7 object support was used.

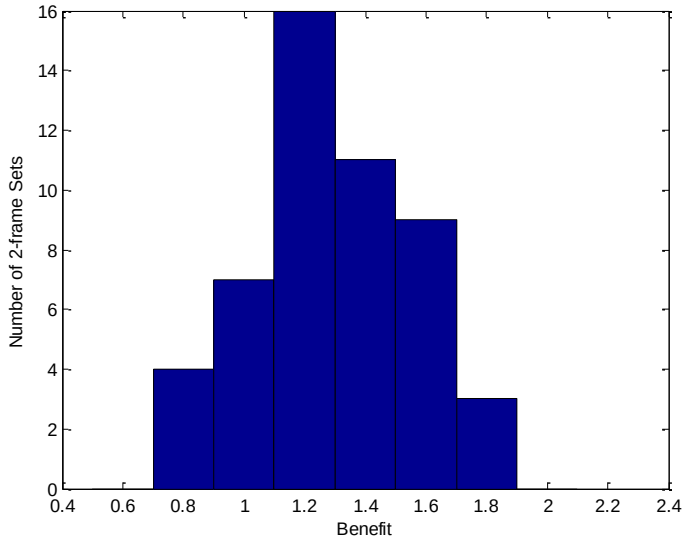

Figure 27. Histogram of the benefits calculated using 50 2-frame sets taken from the "atm" PSF set. Blur7 object support was used in the CRB calculations.

The average benefit of the same 50 2-frame sets using a Blur7 object support constraint is 1.32. The shape of the histogram does not change, but simply shifts to the right on the axis. This is due to the fact that the benefit of adding a 2^{nd} frame increases for every 2-frame set as the size of the object support is increased.

6. CONCLUSIONS AND DIRECTIONS FOR FUTURE WORK

The purpose of the research presented in this thesis was to understand how certain input parameters affected multi-frame blind deconvolution. Specifically, the parameters that were studied were the object and point-spread function supports and the inclusion of multiple measurement frames. The analysis of the object support constraint allowed for an extension of previous work in [7] on non-blind deconvolution.

Cramer-Rao Bound theory was utilized as a metric to analyze the effects on MFBD from the different parameters. The CRBs provide an algorithm-independent tool to gain insight into how different support constraints affect MFBD. Also, these CRBs allow for comparison between non-blind deconvolution and MFBD. CRBs for various imaging scenarios were calculated and the conclusions are presented here. First, the object support was varied and the CRBs were compared to those of non-blind deconvolution. Next, the effect on the MFBD CRBs as a function of varying the PSF support is given. Finally, the inclusion of multiple measurement frames is discussed.

Several conclusions can be made about the nature of MFBD compared to non-blind deconvolution. First, when employing blind deconvolution over non-blind

deconvolution, the CRBs for a given support are always higher. This is true of all the CRBs inside the support. Second, as the size of the support is increased, the blind deconvolution CRBs also increase. Therefore, similar to non-blind deconvolution, using the tightest size support will produce the lowest CRBs. Third, the morphology of the blind deconvolution CRBs differs from the morphology of the non-blind CRBs. In the non-blind case, it is well understood that the morphology of the CRBs is a function of the distance from the edge of the support. Hence, the CRBs are highest in the center of the support and decrease toward. This is not the case, however, for blind deconvolution. Foremost, the morphologies of blind deconvolution CRBs are dependent on the actual PSF. In addition, for all PSFs, the high CRBs are generally clustered toward the true object support.

The CRBs were also analyzed as a function of the point-spread function supports. It was shown that increasing the size of the PSF support did not have a significant impact on the object CRBs. This is true of both the sum of the CRBs and of the morphology of the CRBs. Although the sum of the object CRBs increase as the size of the PSF support is increased, it is relatively small compared to the increase of object CRBs as the size of the object support is increased. Also, as the size of the PSF support is increased, the increase in object CRBs is distributed fairly uniformly across the support. Thus, the morphology of the CRBs does not change. It is more effective to concentrate efforts in providing a smaller object support, as opposed to a smaller PSF support.

Finally, multiple measurement frames were included in the MFBD process. Several conclusions can be made about how these frames affect the MFBD CRBs. First, as more measurement frames are included, the CRBs decrease. Thus, it is advantageous to include as many measurement frames as possible. The properties of the actual PSFs govern the magnitude of decrease in the CRBs for the first few frames. After approximately 8 frames are included, the CRBs decrease as a function of $1/N$, where N is the number of frames. Thus, as more frames are added, the properties of the PSF have less of an impact on the magnitude of the decrease of the CRBs. The effects from using different supports were also analyzed. As the size of the object support is increased, the decrease in the CRBs when adding a particular frame is greater.

The research in this thesis shows that the specific properties of the point spread functions have important impacts on two aspects of MFBD. First, the properties of the PSF govern the morphology of the object CRBs. As a result, they also govern the magnitude of increase of CRBs when employing MFBD over non-blind deconvolution. Second, the properties of the PSF dominate the sum of the CRBs when only a few measurement frames are included. However, it is not known at this time what specific characteristics of these PSFs cause the unexplained phenomena discussed above. Therefore, on-going and future work lies in the research of the impact that specific properties of the PSF have on MFBD.

Also, in order to move the imaging scenario toward more realistic situations, non-invertible PSFs must be used. Therefore, the effects on MFBD from applying

regularization filters must be studied. Also, a photon noise model should be included in the imaging scenario. Further research needs to be conducted to understand the effects of including photon noise on MFBD.

7. LIST OF REFERENCES

[1] R. Bates, "Astronomical speckle imaging," *Phys. Reports*, vol. 90(4), pp. 203-97, Oct. 1982.

[2] T. Wilson and S. J. Hewlett, "Imaging strategies in three-dimensional confocal microscopy," *Proceedings of SPIE* 1245, pp. 35-45, 1991.

[3] V. Krisbnamurthi, Y.-H. Liu, T. Holmes, "Blind deconvolution of 2D and 3D fluorescent micrographs," *Proceedings of SPIE* 1660, pp. 95-102, 1992.

[4] J. Muller, Ed., *Digital Image Processing in Remote Sensing*, pp. 226-269, Philadelphia: Taylor & Francis, 1988.

[5] D. Kundur and D. Hatzinakos, "Blind image deconvolution: an algorithmic approach to practical image restoration," *IEEE Signal Processing Magazine* 13, pp. 43-64, May 1996.

[6] C. Matson and D. Tyler, "Positivity and support: a comparison," *Proceedings of SPIE* 3217, pp. 200-209, 1997.

[7] C. Beckner, "Fundamental limits to noise reduction using support constraints and regularization – A Cramer-Rao bound analysis," *Master's Thesis*, University of New Mexico, 2005.

[8] J. Gorman and A. Hero, "Lower bounds for parametric estimation with constraints," *IEEE Transactions on Information Theory* 26, pp. 1285-1301, 1990.

[9] B. Porat, *Digital Processing of Random Signals – Theory and Methods*, Prentice-Hall, Englewood Cliffs, 1994.

[10] C. Matson and A. Haji, "Cramer-Rao lower bounds for support-constrained and pixel-based mutliframe blind deconvolution," *Proceedings of SPIE* 6365, 2006.

[11] R. LaBelle and S. Garvey, "Introduction to high performance CCD cameras," *Instrumentation in Aerospace Simulation Facilities, 1995. ICIASF '95 Record., International Congress on*, 1995.

[12] J. Janesick, *Scientific Charge-Coupled Devices*, SPIE Press, vol. PM38, Bellingham, WA, 2001.

[13] L. Snyder, A. M. Hammoud, and R. L. White, "Image recovery from data acquired with a charge-coupled-device camera," *J. Opt. Soc. Am. A* 10, 1993.

[14] J. Goodman, *Introduction to Fourier Optics*, Roberts & Company Publishers, Englewood, CO, 2005.

[15] C. McGillem, *Continuous and Discrete Signal and System Analysis*, Saunders College Publishing, New York, 1991.

[16] T. Schulz, "Multiframe blind deconvolution of astronomical images," *J. Opt. Soc. Am. A* 10, 1993.

[17] R Gonzales and R. Woods, *Digital Image Processing*, Prentice-Hall, New Jersey, 2002.

[18] S. Kay, *Fundamentals of Statistical Signal Processing: Estimation Theory*, Prentice-Hall, New Jersey, 1993.

[19] L. Andrews, *Field Guide to Atmospheric Optics*, SPIE Press, vol. FG02, Bellingham, WA, 2001.

[20] M. Born and E. Wolf, *Principles of Optics*, Pergamon Press, Oxford, 1980.

[21] A. Papoulis, *Probability, Random Variables, and Stochastic Processes*, McGraw-Hill, New York, 1965

[22] M. Roggemann and B. Welsh, *Imaging Through Turbulence*, CRC Press, Boca Raton, 1996.

[23] C. Matson, K. Schulze, P. Billings, and D. Tyler, "Multi-frame blind deconvolution and bispectrum processing of atmospherically-degraded data: a comparison," *Proceedings of SPIE* 4792, pp. 55-66, 2002.